Atmospheric
Chemistry
and Physics

Biomass burning combustion efficiency observed from space using measurements of CO and NO_2 by the TROPOspheric Monitoring Instrument (TROPOMI)

Ivar R. van der Velde[1,2], **Guido R. van der Werf**[1], **Sander Houweling**[1,2], **Henk J. Eskes**[3], **J. Pepijn Veefkind**[3,4], **Tobias Borsdorff**[2], **and Ilse Aben**[1,2]

[1]Faculty of Science, VU University, Amsterdam, the Netherlands
[2]SRON Netherlands Institute for Space Research, Utrecht, the Netherlands
[3]KNMI Royal Netherlands Meteorological Institute, De Bilt, the Netherlands
[4]Department of Geoscience and Remote Sensing, Delft University of Technology, Delft, the Netherlands

Correspondence: Ivar R. van der Velde (i.r.vander.velde@vu.nl)

Abstract. The global fire emission inventories depend on ground and airborne measurements of species-specific emission factors (EFs), which translate dry matter losses due to fires to actual trace gas and aerosol emissions. The EFs of nitrogen oxides (NO_x) and carbon monoxide (CO) can function as a proxy for combustion efficiency to distinguish flaming from smoldering combustion. The uncertainties in these EFs remain large as they are limited by the spatial and temporal representativeness of the measurements. The global coverage of satellite observations has the advantage of filling this gap, making these measurements highly complementary to ground-based or airborne data. We present a new analysis of biomass burning pollutants using space-borne data to investigate the spatiotemporal efficiency of fire combustion. Column measurements of nitrogen dioxide and carbon monoxide (XNO_2 and XCO) from the TROPOspheric Monitoring Instrument (TROPOMI) are used to quantify the relative atmospheric enhancements of these species over different fire-prone regions around the world. We find spatial and temporal patterns in the $\Delta XNO_2 / \Delta XCO$ ratio that point to distinct differences in biomass burning behavior. Such differences are induced by the burning phase of the fire (e.g., high-temperature flaming vs. low-temperature smoldering combustion) and burning practice (e.g., the combustion of logs, coarse woody debris and soil organic matter vs. the combustion of fine fuels such as savanna grasses). The sampling techniques and the signal-to-noise ratio of the retrieved

$\Delta XNO_2 / \Delta XCO$ signals were quantified with WRF-Chem experiments and showed similar distinct differences in combustion types. The TROPOMI measurements show that the fraction of surface smoldering combustion is much larger for the boreal forest fires in the upper Northern Hemisphere and peatland fires in Indonesia. These types of fires cause a much larger increase (3 to 6 times) in ΔXCO relative to ΔXNO_2 than elsewhere in the world. The high spatial and temporal resolution of TROPOMI also enables the detection of spatial gradients in combustion efficiency at smaller regional scales. For instance, in the Amazon, we found higher combustion efficiency (up to 3-fold) for savanna fires than for the nearby tropical deforestation fires. Out of two investigated fire emission products, the TROPOMI measurements support the broad spatial pattern of combustion efficiency rooted in GFED4s. Meanwhile, TROPOMI data also add new insights into regional variability in combustion characteristics that are not well represented in the different emission inventories, which can help the fire modeling community to improve their representation of the spatiotemporal variability in EFs.

1 Introduction

The importance of biomass burning as a source of atmospheric trace gases and aerosols has been increasingly stud-

ied and recognized in the past decades (Andreae, 2019). To quantitatively assess the influence of biomass burning on atmospheric chemistry and climate, the atmospheric modeling community requires accurate estimates of fire emissions. Important scientific efforts have led to the development of a number of biomass burning emission products by combining satellite-derived datasets of burned area with biogeochemical models and biomass density datasets that enabled more accurate emission estimates (e.g., Hoelzemann et al., 2004; Ito and Penner, 2004; van der Werf et al., 2003). Since then much progress has been made to reduce uncertainties of the involved datasets (e.g., burned area, fuel loads, combustion factors, and emission factors), but the uncertainties in the emission estimates remain substantial, especially at the more detailed regional scales (van der Werf et al., 2017). The recent emergence of new space-based instruments that measure different trace gases could provide additional top-down constraints on biomass burning emissions and combustion characteristics.

Since the 1980s numerous field measurement campaigns have provided information on biomass burning characteristics and emissions for different biomes and vegetation types around the world (e.g., Andreae et al., 1988; Lacaux et al., 1996; Yokelson et al., 1999). Most of these studies derived so-called emission factors (EF or EFs) for different chemical compounds to quantify the number of grams of a trace gas or aerosol emitted per kilogram of biomass burned. These EFs are combined with biogeochemical models such as used in the Global Fire Emissions Database (GFED; van der Werf et al., 2010) to provide global biomass burning emission estimates, which in turn are used as input for atmospheric transport models (e.g., CarbonTracker data-assimilation system; Peters et al., 2007). The main function of these biogeochemical models is to help predict the spatiotemporal combustion rate of biomass dry matter based on the fuel load, combustion completeness and/or remotely sensed products like burned area or fire radiative power (FRP). A number of EF databases have been published, providing biome-average EFs derived from the large collection of available field and laboratory measurements. The first widely used EF database came from Andreae and Merlet (2001), followed by Akagi et al. (2011), who introduced additional biome categories and selected only measurements of fresh smoke plumes before significant photochemical processes occurred. The latter improved the consistency with atmospheric transport models that use fire emissions as direct inputs before the internal chemistry parameterizations affect the emitted tracers. However, these databases do not account for the variability in EFs within the same biome, which can be substantial and introduces a major source of uncertainty (van Leeuwen et al., 2013). Natural variations in the chemical and structural composition of biomass, temperature, moisture content, and wind speed can cause large variations in the relative fraction of flaming and smoldering combustion. As a consequence, actual EFs may vary substantially, calling for more detailed information to move beyond the use of biome-average values.

The lack of spatial representativeness in EF estimates can partly be resolved by increasing the field measurement effort. In addition, key information on biomass burning characteristics can be retrieved from space-based instruments, as it is reflected in the atmospheric composition of different trace gases. The main advantage of these instruments is the large spatial and temporal coverage that can be achieved, compensating for limitations in spatial resolution and surface sensitivity. Therefore, satellite measurements of regional trace gas enhancements have the potential to provide valuable information on combustion efficiency, burning practices, fuel type and their variability, in particular in remote areas where we lack ground-based measurements and other detailed information. Two trace gases of particular interest are commonly measured from space: carbon monoxide (CO) and nitrogen dioxide (NO_2). Enhanced atmospheric abundances of these two species due to fires provide a unique atmospheric fingerprint of biomass combustion efficiency, i.e., the fraction of biomass combustion by flaming and smoldering. Flaming combustion is hotter and cleaner and produces relatively large amounts of NO_2 and relatively small amounts of CO, whereas smoldering combustion happens at fairly low temperatures at the surface and produces predominantly CO (Andreae and Merlet, 2001).

Previous applications of joint trace gas analysis, including CO and NO_2, focused mostly on constraining anthropogenic and fossil fuel emissions, using either surface observations (e.g., Lopez et al., 2013; Hassler et al., 2016) or satellites (e.g., Silva et al., 2013; Reuter et al., 2014; Konovalov et al., 2016). Mebust and Cohen (2013) demonstrated the detection of seasonal variations of fire EFs in the African savannas using satellite measurements of NO_2. Silva and Arellano (2017) used satellite observations of CO, CO_2 and NO_2 in a novel way to distinguish combustion types around the world. This study provided new insights into emission inventories as they found distinct differences in the ratios of CO/CO_2 and CO/NO_2 between different biomass and urban combustion regions, which are often not well represented in emission inventories.

In this study we aim to demonstrate the capabilities of the new space-borne TROPOspheric Monitoring Instrument (TROPOMI, launched in October 2017; Veefkind et al., 2012) to provide new information about biomass burning characteristics and efficiency in different regions around the globe. The main advantage of TROPOMI is that it delivers co-located column densities of several trace gases, including CO and NO_2. It extends the capability of legacy instruments like MOPITT and OMI by measuring trace gases at improved accuracy, surface sensitivity, and spatial resolution providing daily global coverage. The wealth of data that TROPOMI provides offers the unique opportunity to monitor seasonal changes in the relative amount of flaming and smoldering combustion, even in remote regions where

ground-based measurements of fire properties are sparse. For instance, under relatively clear-sky conditions, the Amazon basin can now be examined for trace gases in much more detail on a day-to-day basis during annual dry season fire spells. TROPOMI surmounts some of the limitations of previous joint trace gas analysis studies where measurements were often taken from various instruments, each with their own intrinsic limitations such as a clear-sky-only retrieval requirement (e.g., with MOPITT) and with widely different spatial resolutions and repeat cycles, i.e., the number of days between two satellite overpasses over the same region. The improved consistency among the different TROPOMI data products in terms of overpass time and location, retrieval sensitivity and spatiotemporal resolution might also help to suppress aggregation errors and biases in the derived ratios of trace gases, improving the capability to distinguish differences in combustion types at the regional scale. The aim of this study is 2-fold: (1) to demonstrate the detection of spatial variations in the regional enhancements of CO and NO_2 for different fire-prone areas that are either dominated by smoldering or flaming fires or a combination of both; (2) to investigate the use of TROPOMI CO and NO_2 to verify the current set of biome-specific EFs used in the atmospheric and climate modeling community.

2 Methodology

2.1 GFED4s and GFAS emission factor ratio

We used two well-established biomass burning emission datasets to interpret and validate TROPOMI-inferred combustion characteristics and efficiencies: the Global Fire Emission Database version 4 with small fires (GFED4s; van der Werf et al., 2017) and the Global Fire Assimilation System version 1 (GFAS; Kaiser et al., 2012). Both datasets provide global fire emission fluxes for a large number of chemical species but use different methods.

GFED4s is based on the Carnegie–Ames–Stanford approach (CASA) biogeochemical model (Potter et al., 1993) to predict the amount of above- and below-ground biomass at monthly temporal resolution. The MODIS Collection 5.1 MCD64A1 500 m burned area satellite product (Giglio et al., 2013) is used to estimate the daily dry matter combustion rate at $0.25° \times 0.25°$ spatial resolution from 2001 up to 2016. GFED4s also includes $1 \times 1 \, km^2$ thermal anomalies (active fire counts) from Terra and Aqua MODIS and $500 \times 500 \, m^2$ surface reflectance observations, providing a statistical estimate of the burned area associated with small fires (Randerson et al., 2012; van der Werf et al., 2017). The GFED4s flux estimates from 2017 onward (used in this study) are not directly derived from the burned area product because the underlying MODIS algorithm was upgraded from Collection 5.1 to Collection 6. Instead, flux estimates are simply derived from MODIS active fire detections and their FRP and the cli-

matological ratio between them derived from the overlapping 2003–2016 period. The GFAS product calculates emissions by assimilating FRP observations from the MODIS Terra and Aqua satellites and is tuned to match the dry matter combustion rate of GFED3 per biome (Kaiser et al., 2012). The version we used provides daily emissions at $0.1° \times 0.1°$ spatial resolution.

Both biomass burning products are combined with EFs to translate the derived dry matter combustion rate to specific trace gas and aerosol emissions. These EFs are based on a large number of trace gas measurement campaigns in the field, in the air or in the laboratory and are subdivided for dominant biome/burning categories without specifying any variability in space and time. GFAS uses the older EF dataset compiled by Andreae and Merlet (2001) with additional updates from the literature and EFs of peatland fires from Christian et al. (2003). In this dataset boreal and temperate forest fires form together a single category named extratropical forest fires (ETFs). GFED4s uses EFs largely based on the dataset compiled by Akagi et al. (2011). This dataset is based on trace gas measurements from fresh smoke sampled in close proximity to the fire source and cooled to ambient temperature but with minimal photochemical processing. This provides a better representation of the initial emissions without chemical disturbances (to aid assessment of biomass burning in atmospheric chemistry models). The Akagi et al. (2011) dataset makes a distinction between boreal and temperate forest fires. For boreal fires they used the average of airborne and ground-based measurements that is roughly equivalent to assuming 70 % of dry matter consumption originates from smoldering combustion. Therefore, the EFs for the boreal latitudes are relatively high for carbon monoxide (EF_{CO}: 127.0 $g \, kg^{-1}$) and low for nitrogen oxides (EF_{NO_x}: 0.9 $g \, kg^{-1}$). The EFs for the temperate fires are 88.0 and 1.9 $g \, kg^{-1}$, respectively, for CO and NO_x and represent a larger fraction of flaming combustion similar to the ETF category used in the Andreae and Merlet (2001) dataset. Other variations in EFs between Akagi et al. (2011) and Andreae and Merlet (2001) are due to variations in the averaging and weighting methods of the measurements. In addition, GFED4s includes sub-grid cell partitioning of burned area to account for different fire types within a grid cell, which affects the grid-average emissions of CO and NO_x. Because NO is usually the most abundant N species emitted into the atmosphere and because NO and NO_2 are rapidly interconverted in the atmosphere, both datasets report EFs for NO_x as NO. Henceforth, the EFs are reported in units of $mmol \, kg^{-1}$ and $mol \, kg^{-1}$ for EF_{NO_x} and EF_{CO}, respectively, to make ratios of EFs of similar magnitude to the ratios of column densities measured by TROPOMI (see Sect. 2.2). Table 1 shows an overview of EFs of CO and NO_x used by GFAS and GFED4s.

The spatial stratification of the different biomass burning categories is apparent in the ratio between NO_x and CO EFs. This ratio exhibits a distinct "fingerprint" that carries infor-

Table 1. Emission factors for NO_x (emitted as NO) and CO used by GFED4s (mostly based on Akagi et al., 2011, and a few other sources) and GFAS (mostly based on Andreae and Merlet, 2001, with additional updates) for different types of biomass burning. The final two columns on the right show the ratio between EF_{NO_x} and EF_{CO} (EFR) for the two emission databases. The original units $(g\,kg^{-1})$ are converted to $mmol\,kg^{-1}$ and $mol\,kg^{-1}$ for EF_{NO_x} and EF_{CO}, respectively, to make units of EFR equal to TROPOMI mole density ratios.

	EF_{NO_x} $(mmol\,kg^{-1})$		EF_{CO} $(mol\,kg^{-1})$		$EFR = EF_{NO_x} / EF_{CO}$	
	GFED4s	GFAS	GFED4s	GFAS	GFED4s	GFAS
Peat fires	33.33	33.33	7.50	7.50	4.44	4.44
Boreal forest fires	30.00	–	4.54	–	6.61	–
Temperate forest fires	64.00	–	3.14	–	20.38	–
Extratropical fires	–	113.33	–	3.79	–	29.90
Tropical deforestation fires	85.00	82.14	3.32	3.61	25.60	22.75
Agricultural waste burning	103.67	82.14	3.64	3.29	28.48	24.97
Savanna fires	130.00	70.00	2.25	2.18	57.78	32.11

mation on combustion efficiency, combustion practice, and fuel type. In this study, we call this dimensionless metric the emission factor ratio ($EFR = EF_{NO_x} / EF_{CO}$). EFR is a relative measure of how many millimoles of NO_x are released into the atmosphere for each mole of CO. This metric is a proxy for the modified combustion efficiency (MCE) parameter that is often used in fire emission quantification studies but is more difficult to derive from space given the relatively small departures of CO_2 concentrations over biomass burning regions from background conditions. The MCE is defined as $\Delta CO_2 / (\Delta CO + \Delta CO_2)$ to indicate combustion efficiency of a fire by measuring the amount of excess in CO_2 in comparison to total emitted C from CO_2 and CO (Yokelson et al., 1999). Table 1 gives the EFR for the different combustion types based on the ratio between the EFs of NO_x and CO used by GFED4s and GFAS. Figure 1a and b show the spatial distributions of EFR in both datasets. For GFED4s, we subdivided EFR into three different categories: high EFR above 50 for savanna fires, EFR between 10 and 50 for temperate forest fires, tropical deforestation fires and agricultural waste burning, and EFR lower than 10 for boreal and peatland fires. High EFR is thus related to the flaming type of combustion that is hotter and more efficient as it produces relatively less CO alongside CO_2 and relatively more NO_x by combustion of N in the biomass itself. Conversely, low EFR is generally related to slow smoldering type of combustion. The EFR categories are similar for GFAS; however, due to differences between the EFs datasets (for reasons discussed in the previous paragraph), EFRs are classified differently: high EFR above 30 for savanna fires, EFR between 10 and 30 for ETF fires, tropical deforestation fires and agricultural waste burning, and EFR lower than 10 for peatland fires.

Highlighted in Fig. 1 are various regions of interest studied in this paper with strong seasonal occurrences of biomass burning. Regions that have been selected for detailed analysis using TROPOMI are 2 boreal fire regions in North America, 1 boreal fire region in Siberia, 5 savanna fire regions on the African continent, 1 savanna fire region in Australia, 2 peat-

land fire regions in Indonesia, and 15 regions in South America to more specifically study spatial gradients in combustion efficiency between tropical deforestation and savanna fires.

2.2 TROPOMI CO and NO_2

The TROPOMI instrument was launched on 13 October 2017 onboard the Sentinel-5 Precursor satellite to monitor the chemical composition of the atmosphere (Veefkind et al., 2012). It measures a range of trace gases at unprecedented spatial resolution with a daily global coverage. Section 2.2.1 and 2.2.2 provide further details about the TROPOMI operational level-2 column density data products of carbon monoxide (XCO) and nitrogen dioxide (XNO$_2$). Figure 2 shows a few examples of monthly and daily average maps of XCO and XNO$_2$ for a number of biomass burning regions together with CO emissions from GFED4s (Sect. 2.1). Enhancements in XCO and XNO$_2$ correspond well to local fire emissions based on an independently derived burned area. Note that the chemical lifetime of NO_x is much shorter than for CO (minutes to hours vs. weeks to months). The main chemical driver during daytime is the photochemical balance between NO_2 photolysis and NO oxidation by ozone converting NO into NO_2 and makes NO_2 a robust measure for NO_x. The NO_x lifetime is limited by the conversion of NO_2 to HNO_3 in reaction with hydroxyl (OH) radicals. The short chemical lifetime results in a precise alignment between the enhancements of XNO$_2$ and the location of fire emissions, while enhancements of XCO are more affected by atmospheric transport due to its longer chemical lifetime. These differences in lifetime can cause biases in the joint analysis of XNO$_2$ and XCO and its ratio. That limits our ability to make direct quantitative comparisons between EFs and column densities. Nonetheless, assuming the lifetime does not vary greatly from fire to fire and from region to region, it is probable that it does not affect our ability to detect variations in fire characteristics around the world. This limitation is further discussed in Sect. 4 of the paper.
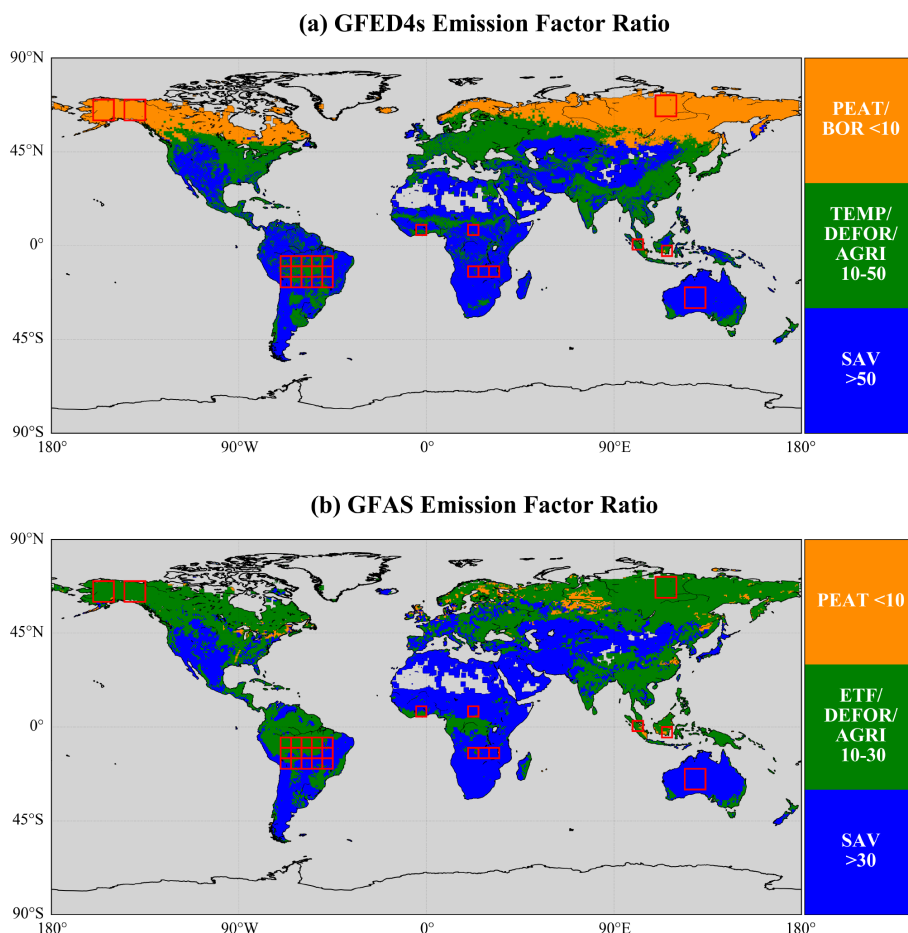
(a) GFED4s Emission Factor Ratio

(b) GFAS Emission Factor Ratio

Figure 1. Emission factor ratio between NO_x and CO (EFR) for GFED4s **(a)** and GFAS **(b)**. In panel **(a)** the range of EFR values is subdivided into three aggregated fire-type categories: (1) peat and boreal fires (PEAT/BOR: < 10), (2) temperate forest, deforestation and agricultural fires (TEMP/DEFOR/AGRI: between 10 and 50) and (3) savanna fires (SAV: > 50). In panel **(b)** the range of EFR values subdivided along a different classification (see Sect. 2.1): (1) peat fires (PEAT: < 10), (2) extratropical forest, tropical deforestation and agricultural fires (ETF/DEFOR/AGRI: between 10 and 30), and (3) savanna fires (SAV: > 30). Regions of interest are highlighted by the red boxes.

2.2.1 XCO

The carbon monoxide total column density from TROPOMI is retrieved from reflected and backscattered solar radiance around 2.3 µm measured by the shortwave infrared module of the spectrometer. The Shortwave Infrared Carbon Monoxide Retrieval algorithm (SICOR, Landgraf et al., 2016) is used to translate spectral radiances to XCO column densities, with high sensitivity to the planetary boundary layer for clear-sky conditions over land. For cloudy conditions over land and ocean, the XCO has a stronger sensitivity at higher altitude. To account for cloud interferences SICOR retrieves an effective cloud optical depth and cloud height and provides a column averaging kernel as part of the product which represents the height sensitivity of the measurement.

A good agreement was found between TROPOMI XCO and TCCON XCO ground measurements for clear- and cloudy-sky conditions (Borsdorff et al., 2018a). Mean biases amount to 6.0 ppb for clear-sky retrievals, 6.2 ppb for cloudy-sky retrievals and 5.8 ppb for the combination of both. The station-to-station standard deviation of the bias was 3.9 ppb for clear-sky, 2.4 ppb for cloudy-sky, and 2.9 ppb for the combination of both. Thereby, TROPOMI achieves its mission requirements on precision ($< 10\%$).

The XCO column density for 2018 is observed with daily global coverage at a spatial resolution of $7 \times 7\,\mathrm{km}^2$ in nadir. The data are selected for clear-sky and cloudy-sky conditions with a cloud top height limited to 5000 m and an aerosol optical thickness equal to or larger than 0.5 (TROPOMI CO level-2 README document; Landgraf et al., 2018). In addition, the two most westward pixels of the swath were excluded due to performance issues (Borsdorff et al., 2018b). The XCO column density is presented in units of mole per square meter ($\mathrm{mol\,m^{-2}}$).

2.2.2 $X\mathrm{NO}_2$

The tropospheric nitrogen dioxide column density from TROPOMI is retrieved from spectrometer measurements of direct and backscattered solar radiance between 405 and 465 nm. The $X\mathrm{NO}_2$ retrieval algorithm uses the DOAS approach and is an adapted version of the algorithm used for the DOMINO v2.0 (Boersma et al., 2011) and QA4ECV $X\mathrm{NO}_2$ products (van Geffen et al., 2015; Boersma et al., 2018). In the retrieval procedure, NO_2 slant columns are derived from the measured spectra using the DOAS method. Then the tropospheric component of the slant columns is separated from the stratospheric component, and finally the tropospheric slant columns are converted to vertical columns $X\mathrm{NO}_2$ based on the tropospheric air mass factor (AMF).

$X\mathrm{NO}_2$ is observed with daily global coverage at a spatial resolution of $3.5 \times 7\,\mathrm{km}^2$ in nadir. The spectrometer's near-infrared band provides additional information on cloud characteristics and allows a better cloud correction, i.e., improving the measurement precision under cloudy conditions. $X\mathrm{NO}_2$ column densities have been compared with ground-based MAX-DOAS measurements at 14 stations. In general, TROPOMI underestimates the tropospheric column at polluted sites. The daily median negative biases are generally less than 50 %, within the required measurement precision, but vary from station to station (TROPOMI NO_2 level-2 README document; Eskes and Eichmann, 2018). Because this bias is largely systematic, it is not expected to deteriorate our ability to differentiate between fire characteristics. This is further investigated in Sect. 3.2.

For this study, we use the recommended filter settings outlined in the README document, removing cloud-covered scenes with a cloud radiance fraction exceeding 0.5, scenes covered by snow or ice, and other problematic retrievals (qa_value > 0.75). The $X\mathrm{NO}_2$ column density is presented in units of millimole per square meter (mmol m^{-2}).

2.3 Mole fraction ratio: sampling methods

For our analysis, we selected important hotspots of biomass burning according to the GFED4s database. To prevent contamination with urban trace gas emissions, large population centers were avoided. The regions are outlined in Figs. 1 and 2. Within each region we collected all the available $X\mathrm{CO}$ and $X\mathrm{NO}_2$ data that passed the filters explained in Sect. 2.2.1 and 2.2.2 for up to 3 consecutive months depending on the timing and duration of the fire season.

To derive the regional enhancements in $X\mathrm{CO}$ and $X\mathrm{NO}_2$ relative to the background, $\Delta X\mathrm{CO}$ and $\Delta X\mathrm{NO}_2$, respectively, we used two main sampling methods depending on the scale and severity of the fires in the region. A statistical bulk method (SBM) is used for regions that are characterized by extensive seasonal burning over a large area and where upwind background levels of $X\mathrm{CO}$ and $X\mathrm{NO}_2$ are difficult to define. A local sampling method (LSM) is used for regions

where we could identify local fires and plumes of enhanced trace gas abundance for which the wind direction and background column density upwind of the fires could be determined. Each method is discussed in more detail in Sect. 2.3.1 and 2.3.2, respectively. With daily estimates for $\Delta X\mathrm{NO}_2$ and $\Delta X\mathrm{CO}$ we were able to derive a new dimensionless metric: the mole density ratio (MDR = $\Delta X\mathrm{NO}_2 / \Delta X\mathrm{CO}$). The MDR is the atmospheric equivalent of EFR and provides a remotely sensed proxy for biomass combustion efficiency.

2.3.1 Statistical bulk method

The SBM is based on the method discussed in Silva and Arellano (2017), who used it to distinguish urban and industrial trace gas enhancements from biomass burning. It provides a simple measure of regional trace gas enhancements when background column densities are difficult to determine. For this method, the daily TROPOMI data were regridded at $0.1° \times 0.1°$ resolution from which co-located $X\mathrm{CO}$ and $X\mathrm{NO}_2$ data within $5° \times 5°$ boxes were sampled each day over the selected regions (see Figs. 1 and 2). The size of these boxes allows for a sufficient number of trace gas observations each day (more than 1000). To determine the regional trace gas enhancement relative to the background ($\Delta X\mathrm{CO}$ and $\Delta X\mathrm{NO}_2$ are here jointly indicated by ΔX), we assume that the sampled data exhibit a Gaussian normal distribution. A trace gas enhancement of 1 standard deviation above the daily mean of the distribution is assumed to be due to fires, i.e., $X_{\mathrm{fire}} = \mu_X + \sigma_X$. Conversely, a column density of 1 standard deviation below the mean is assumed to represent the trace gas background, i.e., $X_{\mathrm{BG}} = \mu_X - \sigma_X$. This implies that the regional trace gas enhancement is assumed to be 2 times the standard deviation of the distribution, i.e., $\Delta X = X_{\mathrm{fire}} - X_{\mathrm{BG}} = 2\sigma_X$. Figure 3a displays an idealized normal distribution of sampled column densities of $X\mathrm{CO}$ indicating the values of $X\mathrm{CO}_{\mathrm{fire}}$, $X\mathrm{CO}_{\mathrm{BG}}$, $\Delta X\mathrm{CO}$, $\mu_{X\mathrm{CO}}$, and $\sigma_{X\mathrm{CO}}$ along the distribution. The MDR between $\Delta X\mathrm{NO}_2$ and $\Delta X\mathrm{CO}$ is therefore equal to the ratio between 2 standard deviations $\sigma_{X\mathrm{NO}_2}/\sigma_{X\mathrm{CO}}$. As discussed by Silva and Arellano (2017), this assumption is only valid if both species are highly correlated with each other. This is the case for this study given the strong co-location of the sampled $X\mathrm{CO}$ and $X\mathrm{NO}_2$ data, the daily sampling interval for both species, and because we carefully selected strong biomass burning source regions. The SBM was used for the following regions: 15 regions over the southern Amazon basin of South America, where data were sampled between July and September 2018, 2 regions over northern Africa, where data were sampled in December 2018, and 3 regions over southern Africa, where data were sampled between July and September 2018. Deriving ΔX as outlined above may not reflect a formally correct estimate of the regional trace gas enhancement relative to the actual background, but that is also not our main goal. The purpose is to have a consistent method among the two trace gases that provides a reasonable proxy for regional fire-
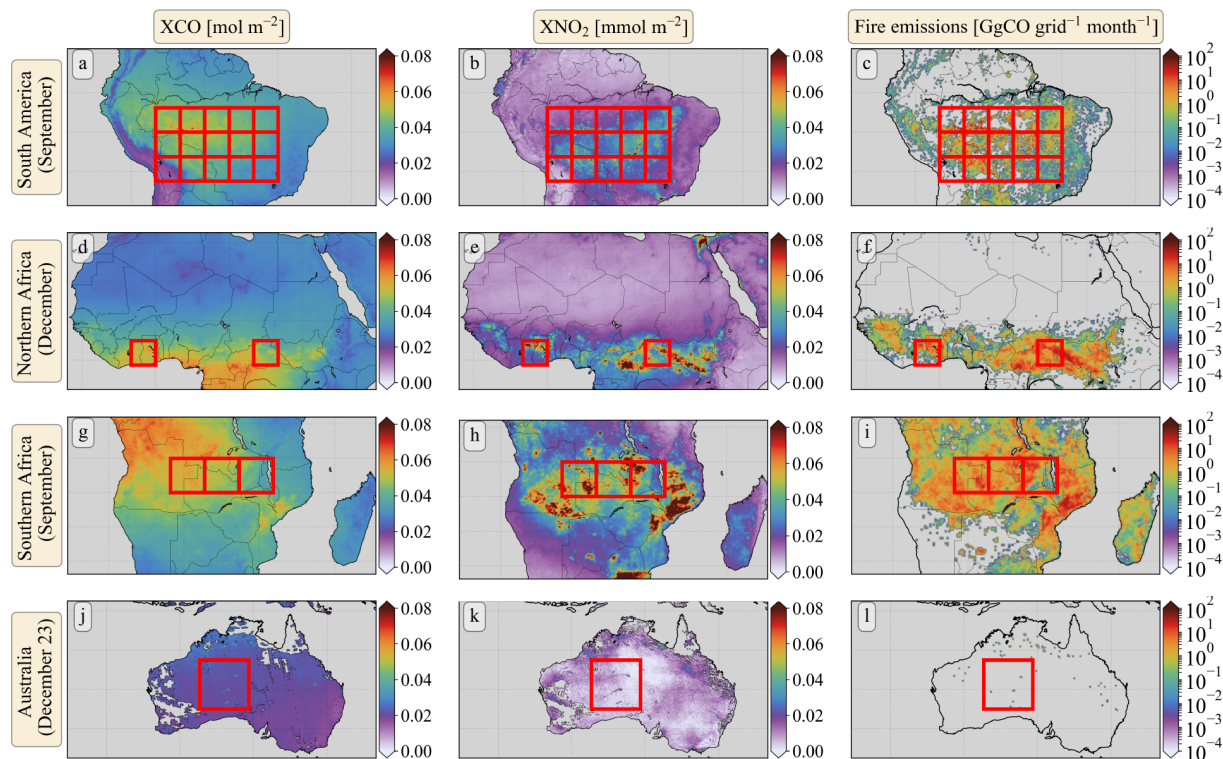
Figure 2. Maps of monthly average XCO (mol m^{-2}), XNO$_2$ (mmol m^{-2}), and GFED4s CO emissions (Gg CO grid^{-1} month^{-1}) for South America **(a–c)**, for northern Africa **(d–f)**, and for southern Africa **(g–i)**. Maps of daily average XCO, XNO$_2$ and GFED4s CO emissions are shown for Australia for 23 December 2018 **(j–l)**. Regions of interest are highlighted by the red boxes.

induced column enhancements. Therefore, this method was only used for regions where we have a very high density of fires within our study area and where it is difficult to investigate individual fire plumes and their background mole density levels. Some of the errors introduced by this method are systematic and have a similar impact on ΔXNO$_2$ and ΔXCO (e.g., error due to atmospheric transport) and will cancel out in the estimate of MDR. Other errors may introduce new uncertainties and biases on top of the TROPOMI column uncertainty unevenly between XNO$_2$ and XCO, potentially affecting our ability to differentiate between combustion characteristics. For instance, the assumption of a Gaussian normal distribution of the sampled data might not hold for one or both of the trace gases. To assess the importance of these uncertainties, we developed two alternative methods to derive ΔX that are closely related to the SBM. The first alternative method (SBM_alt1) assumes that ΔX is not determined by the standard deviation but by the difference between the 15.9 and 84.1 percentile ranks around the median of the distribution. Figure 3b shows an example of such a distribution. Only if the sampled data are perfectly normally distributed will SBM_alt1 and the SBM yield the same result because the two percentile ranks will align with the minus 1 and plus 1 standard deviations. Variations from the standard normal could for instance deteriorate our ability to differentiate between

combustion characteristics as it will affect the estimates for ΔX and MDR. The second alternative method (SBM_alt2) derives ΔX by taking the difference between X_{fire} from the standard SBM and an alternative X_{BG} derived from a distribution of samples from an adjacent $5° \times 5°$ region. Naturally that means the SBM_alt2 ΔX value is only identical to the standard SBM ΔX value if both estimates for X_{BG} are identical. Figure 3c shows an example of this method with an idealized background and source distribution of sampled XCO.

The SBM and the two alternative methods have been validated for two source regions in South America (see Sect. 3.2). The first region is located south of the Amazon River over the Brazilian state of Amazonas in the tropical rainforest and is dominated by deforestation fires, i.e., the practice of burning logs and debris that remain on the landscape after initial clearing to create new agricultural land. The second region is located over the central Brazilian state of Goias in an ecoregion called the Cerrado, which is a savanna-like fire-adapted ecosystem with frequent fires that mostly consume the grass layer but where the expansion of agriculture is also an important cause of fires. These two areas are shown in Fig. 4 in green and blue, respectively. In the 3-month dry season between July and September 2018, the parameters X_{fire}, X_{BG}, and ΔX were determined every

day for XCO and XNO$_2$ using the SBM, SBM_alt1, and SBM_alt2. The latter method used the two adjacent background regions shown in purple in Fig. 4. These two background regions were chosen for a number of reasons. First of all, the background region for the Cerrado savanna fires was on average upwind of the source area. The average wind direction in the planetary boundary layer of the domain was predominantly from the east during the 3-month period (see Fig. 4), based on a WRF-Chem simulation nudged to NCEP re-analysis boundary conditions. Moreover, the CO and NO$_x$ emissions from fires were about 2 times smaller in the background region than in the source region according to the GFED4s database (0.6 Gg CO region^{-1} d^{-1} vs. 1.1 Gg CO region^{-1} d^{-1}). Similarly, we opted for a "clean-air" background area just northeast of the deforestation region where CO and NO$_x$ emissions from fires were very small during our study period.

2.3.2 Local sampling method

The LSM is a more straightforward approach to determine local enhancements in trace gas densities in close proximity to the actual fire hotspot. This method was specifically used for fires in the North American boreal biome in July 2018, the Siberian boreal biome in July and August 2018, the central Australian savanna biome in November and December 2018, and the Indonesian peatland biome in August and September 2018 (see Figs. 1 and 2). All events were relatively isolated from other fires, a prerequisite for using this method. For predefined 5° × 5° and 10° × 10° boxes, TROPOMI data were regridded at 0.1° × 0.1° resolution. Subsequently, co-located XCO and XNO$_2$ data each day are sampled within a radius of 10 km from a location where CO and NO$_x$ were emitted according to GFED4s. For each fire hotspot, X_{fire} is defined as the average of these sampled column densities. The background column density X_{BG} is determined each day by taking the average of all sampled column densities inside a smaller subregion upwind of the fire hotspot within the larger predefined box. The location of the background subregion was determined by visual inspection, looking at the predominant direction of the individual trace gas plumes. For each day, we averaged ΔXCO and ΔXNO$_2$ over active hotspots in the predefined boxes, which were subsequently used to derive a daily average MDR. Days with insufficient data upwind of the fire hotspots were excluded from the analysis as well as days with enhanced trace gas levels that were advected into the region from outside. For instance, we had to filter out by visual inspection a number of days for the North American regions because high amounts of CO were advected from the Eurasian continent to Alaska, obscuring most of the local enhancements in CO.

We show in Fig. 5a and b an example of TROPOMI XCO and XNO$_2$ measured over Australia for 23 December 2018, regridded at 0.1° × 0.1° resolution. The plumes of XCO and XNO$_2$ that start at a number of hotspots and move in a west-

ward direction are easily recognizable. The background region for this particular day is located in the eastern part of the domain upwind of the hotspots (shown by the purple box). The hotspots are positively identified as fires because their locations correspond very accurately to the locations of GFED4s and GFAS fire emissions (depicted by "+" signs). One hotspot located in the westernmost part of the domain (west of 126° E) is not visible in TROPOMI XCO and XNO$_2$. The fire was likely short-lived and only detected in the morning with the MODIS Terra satellite (local 10:30 overpass), 3 h before the TROPOMI overpass. For the other hotspots, Fig. 5a and b show a good correlation between the magnitude of the trace gas enhancements, the plume distances, and the spatial extent and magnitude of the fire emissions.

2.4 WRF-Chem

To evaluate the methodology of the joint analysis of TROPOMI XCO and XNO$_2$, and in particular the SBM sampling technique, we used the Weather Research Forecasting model version 4.0 coupled with chemistry (WRF-Chem). The main purpose was to investigate whether the sampling techniques can provide estimates of XCO, XNO$_2$ and MDR that are distinctly different between four combustion types. Synthetic WRF-Chem simulations were performed using a single domain located over the northern part of South America stretching over 6000 km in the east–west direction and 3900 km in the north–south direction (see Fig. 4). We used a horizontal resolution of 30 × 30 km^2 with 32 vertical levels. We chose the "tropical" suite of physics options that includes the Yonsei University (YSU) scheme for planetary boundary layer physics (Hu et al., 2013), WSM six-class scheme for microphysics (Hong and Lim, 2006), Tiedtke scheme for cloud physics (Tiedtke, 1989), and rapid radiative transfer method (RRTM, Mlawer et al., 1997) for shortwave and longwave radiation. We included gas-phase chemistry mechanisms from the Regional Acid Deposition Model version 2 (Stockwell et al., 1990) but without aerosol chemistry. Boundary and input meteorological fields for September 2018 came from the NCEP FNL Operational Global Analysis dataset prepared on a 1° × 1° grid every 6 h. Boundary and initial trace gas concentrations were taken from the CAMS model and were interpolated to WRF vertical levels. GFED4s (see Sect. 2.1) provided the biomass burning dry matter combustion rate based on real fire events for South America in September 2018. These were multiplied by a set of EFs to acquire a synthetic estimate of biomass burning emissions for the entire domain that is associated with a single combustion type: either boreal fires, mixed peat fires, tropical deforestation fires or savanna fires. For the EFs of the mixed peat fires we assumed 60 % is combusted by tropical deforestation (to mimic overstory consumption) and 40 % is combusted by peat soils. As a consequence, each of these four emission estimates carried a different (but in space con-
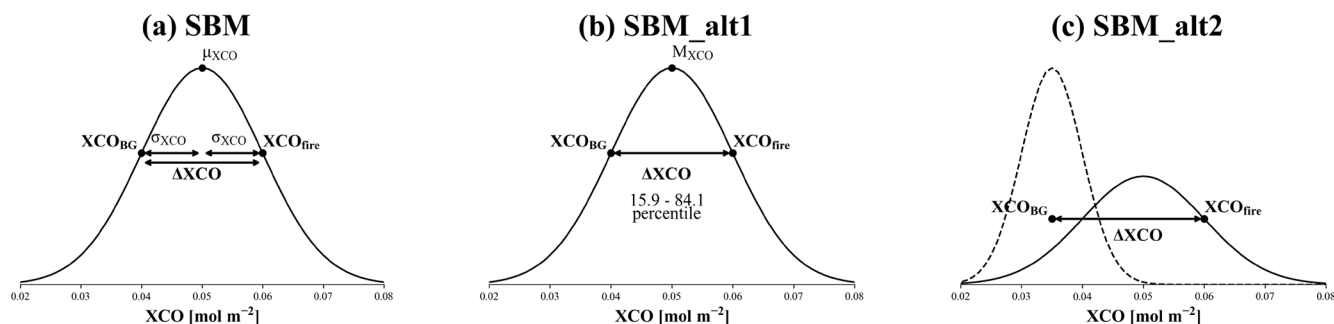
Figure 3. Three types of the statistical bulk method (SBM) are applied to an idealized distribution of XCO samples (mol m^{-2}). In panel (a) the standard SBM where ΔXCO (XCO$_{\text{fire}}$ − XCO$_{\text{BG}}$) is equal to $2\sigma_{X\text{CO}}$ around the distribution mean $\mu_{X\text{CO}}$. In panel (b) the first alternative SBM (SBM_alt1) where ΔXCO is equal to the difference between the 84.1 percentile rank and the 15.9 percentile rank around the median $M_{X\text{CO}}$. The estimates for ΔXCO from the SBM and SBM_alt1 are only equal if the distributions are perfectly Gaussian. In panel (c) the second alternative SBM (SBM_alt2) where ΔXCO is equal to the difference between XCO$_{\text{fire}}$ from the standard SBM and XCO$_{\text{BG}}$ derived from the mean concentration of another XCO distribution sampled upwind of the fire region (dashed distribution). The estimates for ΔXCO from the SBM and SBM_alt2 are only equal if XCO$_{\text{BG}}$ are the same.

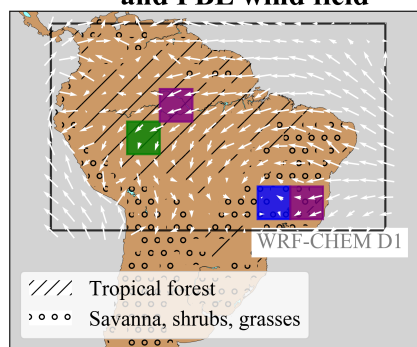**Figure 4.** Location of the deforestation $5° \times 5°$ sampling region (green), the savanna $5° \times 5°$ sampling region (blue) and two background regions adjacent to the two source regions (purple). The WRF-Chem domain and the predominant wind direction in the PBL during the 2018 fire season are superimposed. The location of the green region is also used to sample XCO and XNO$_2$ data from four WRF-Chem simulations (see Sect. 2.4).

stant) EFR between NO$_x$ and CO over the entire domain for each of the respective fire types. In addition, we used a spatial characterization of injection height profiles based on space-based stereo-height information from smoke plumes (Martin et al., 2018).

WRF-Chem was executed four times for September 2018 under the exact same conditions and settings described above, except that we used for each run one of the four modified biomass burning emissions. Each simulation provided hourly three-dimensional fields of CO and NO$_2$ concentrations for the entire month. Close to the center of the domain we collected within a $5° \times 5°$ region each day at 14:00 local time (half an hour later than the actual TROPOMI overpass) all CO and NO$_2$ data. These were translated into XCO and

XNO$_2$ column mole densities using a daily mean estimate of TROPOMI's averaging kernel (AK) of the two respective species, derived from September 2018 data over the same $5° \times 5°$ collection region. This ensured realistic differences in column sensitivity for simulated XCO and XNO$_2$, even under cloudy conditions. The collection of column densities was used to derive daily ΔXCO, ΔXNO$_2$, and MDR using the three SBM sampling methods discussed in Sect. 2.3.1.

3 Results

In Sect. 3.1 we provide an overview of all retrieved MDR signatures and compare them with the regional patterns in EFR and with WRF-Chem simulations. In Sect. 3.2 we present a detailed analysis of XCO and XNO$_2$ data focusing on the Amazon basin. This analysis includes the errors associated with the different sampling methods, the significance of the retrieved MDR signatures in relation to the instrument precision of TROPOMI, and a comparison of retrieved MDR signatures between TROPOMI and two biomass burning datasets.

3.1 Global fire characteristics

By combining ΔXCO and ΔXNO$_2$ data from all investigated regions we can identify a four-way split in regional combustion activity and efficiency (see Fig. 6a and Table 2). According to the TROPOMI data, there is a group of boreal and peatland regions that emit relatively much CO per gram of NO$_x$ in comparison to the other regions and that are in the literature typically characterized as smoldering fires. For these regions we determined MDR values ≤ 1.4. At the opposite end of the spectrum are the savanna regions on three different continents that emit relatively much NO$_x$ generated from nitrogen in the biomass and possibly from thermal decomposition of atmospheric N$_2$ at very high combustion tem-
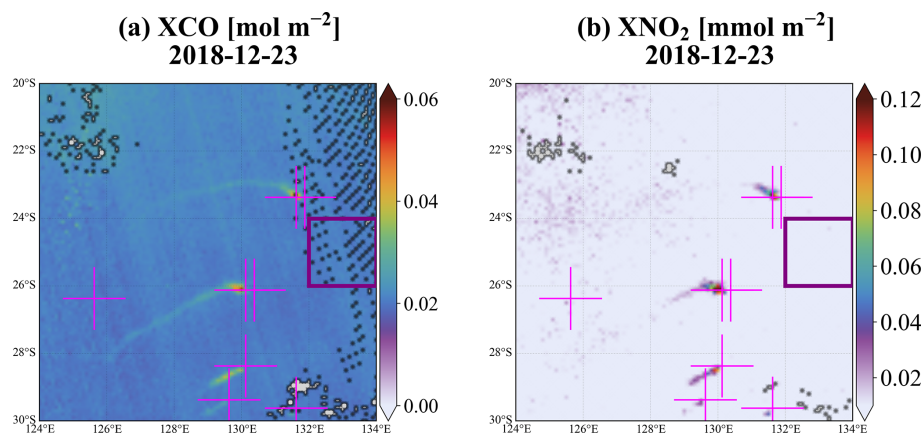
(a) XCO [mol m^{-2}]
2018-12-23

(b) XNO$_2$ [mmol m^{-2}]
2018-12-23

Figure 5. The column density XCO (mol m^{-2}) in panel **(a)** and XNO$_2$ (mmol m^{-2}) in panel **(b)** measured with TROPOMI on 23 December 2018 over central Australia. The background region is depicted by the purple frame and is located upwind of multiple fire plumes. The locations of the GFED4s/GFAS fire emissions are depicted by the magenta plus signs.
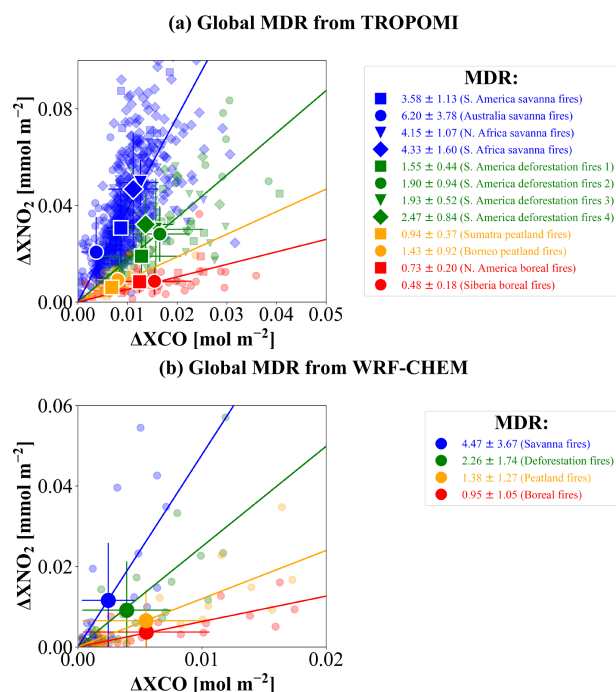

(a) Global MDR from TROPOMI

MDR:
- 3.58 ± 1.13 (S. America savanna fires)
- 6.20 ± 3.78 (Australia savanna fires)
- 4.15 ± 1.07 (N. Africa savanna fires)
- 4.33 ± 1.60 (S. Africa savanna fires)
- 1.55 ± 0.44 (S. America deforestation fires 1)
- 1.90 ± 0.94 (S. America deforestation fires 2)
- 1.93 ± 0.52 (S. America deforestation fires 3)
- 2.47 ± 0.84 (S. America deforestation fires 4)
- 0.94 ± 0.37 (Sumatra peatland fires)
- 1.43 ± 0.92 (Borneo peatland fires)
- 0.73 ± 0.20 (N. America boreal fires)
- 0.48 ± 0.18 (Siberia boreal fires)

(b) Global MDR from WRF-CHEM

MDR:
- 4.47 ± 3.67 (Savanna fires)
- 2.26 ± 1.74 (Deforestation fires)
- 1.38 ± 1.27 (Peatland fires)
- 0.95 ± 1.05 (Boreal fires)

Figure 6. In panel **(a)**, the relationship between daily $\triangle X$CO (mol m^{-2}) and $\triangle X$NO$_2$ (mmol m^{-2}) from TROPOMI combined for all regions of this study. The region average relationship between $\triangle X$CO and $\triangle X$NO$_2$ is depicted by the big markers together with error bars to indicate the 1σ day-to-day variability. The four regression slopes with intercept at zero signify the different groupings of combustion efficiency. The legend includes the average MDR and 1σ day-to-day variability estimates for each region. For the South American deforestation regions, we used data in September, at the height of the 2018 fire season. In panel **(b)**, the relationship between daily $\triangle X$CO and $\triangle X$NO$_2$ and the monthly average MDR from four different synthetic WRF-Chem simulations (see Sect. 2.4).

peratures. The MDR values for savanna fires are much higher than for the boreal and peatland fires and range between 3.6 and 6.2 among the different savanna regions and sampling methods (SBM for South America and Africa, LSM for Australia). In between these two extremes lie four different South American deforestation regions with MDR values that range between 1.6 and 2.5, which is less efficient than the savanna combustion but still more efficient than boreal and peat combustion. In particular for the boreal regions we observe a 3 to 6 times larger increase in $\triangle X$CO relative to $\triangle X$NO$_2$ than for the deforestation and savanna regions. It consistently translates to a much lower monthly average MDR (< 1) for the boreal fires on two different continents, with higher MDR values over boreal North America compared to boreal Siberia.

A similar four-way split in regional combustion characteristics is shown in Fig. 6b using the four synthetic WRF-Chem simulations, each driven by a different set of modified biomass burning emissions to mimic different ecosystems with frequent occurring fires (see Sect. 2.4). The estimates in $\triangle X$CO and $\triangle X$NO$_2$ were derived with the SBM and, while day-to-day variability is quite substantial just like in the real TROPOMI data in Fig. 6a, it demonstrates that the SBM can provide a robust monthly average estimate of MDR. The MDR estimates and the relative differences between the four different fire types compare quite well with the actual derived signals in TROPOMI. The simulated savanna fires have consistently the highest MDRs, which are about twice as high as the simulated tropical deforestation fires and 3 to 4 times as high as the simulated peatland and boreal fires, respectively.

The pattern of combustion signatures in MDR determined with TROPOMI across the different fire types compares well with the spatial patterns in GFED4s EFR (see Fig. 7a). The Pearson correlation coefficient between estimates of MDR and EFR across the five continental areas implies that a strong linear relationship exists ($r = 0.90$). It demonstrates

Table 2. For each region the average mole density ratio (MDR) derived from TROPOMI and WRF-Chem data and the ratio between $\mathrm{EF}_{\mathrm{NO}_x}$ and $\mathrm{EF}_{\mathrm{CO}}$ (EFR) for the GFED4s and GFAS emission databases. The MDR 1σ standard deviation depicts day-to-day variability.

| Type of fire	Region	$X\mathrm{NO}_2/X\mathrm{CO}$ MDR TROPOMI	EFR $\mathrm{EF}_{\mathrm{NO}_x}/\mathrm{EF}_{\mathrm{CO}}$ (GFED4s)	EFR $\mathrm{EF}_{\mathrm{NO}_x}/\mathrm{EF}_{\mathrm{CO}}$ (GFAS)
Savanna fires	Australia	6.20 ± 3.78	57.78	32.24
	South America	3.58 ± 1.13	48.35	26.82
	Northern Africa	4.15 ± 1.07	55.27	31.62
	Southern Africa	4.33 ± 1.60	56.34	31.64
	WRF-Chem	4.47 ± 3.67	57.78	
Deforestation fires	South America 1	1.55 ± 0.44	30.29	20.87
	South America 2	1.90 ± 0.94	40.29	22.13
	South America 3	1.93 ± 0.52	30.89	20.87
	South America 4	2.47 ± 0.84	37.68	23.01
	WRF-Chem	2.26 ± 1.74	25.60	
Peatland fires	Sumatra	0.94 ± 0.37	15.67	14.30
	Borneo	1.43 ± 0.92	9.75	4.70
	WRF-Chem	1.38 ± 1.27	12.89	
Boreal fires	North America	0.73 ± 0.20	6.47	30.11
	Siberia	0.48 ± 0.18	6.53	30.11
	WRF-Chem	0.95 ± 1.05	6.61	
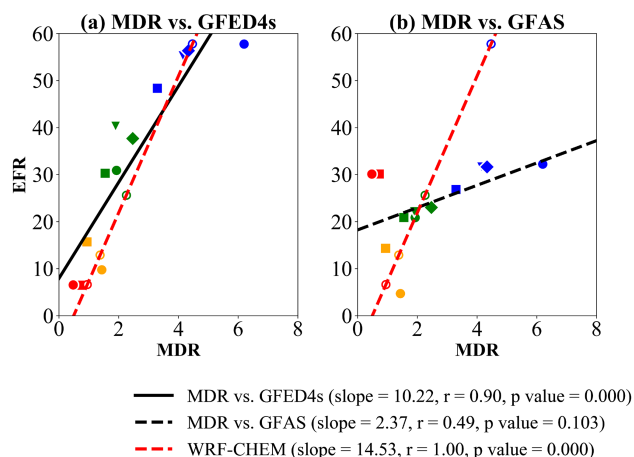
Figure 7. The relationship between the average MDR and EFR from GFED4s is shown in panel **(a)** and between the average MDR and EFR from GFAS in panel **(b)**. The different colored symbols correspond to regions listed in the legend of Fig. 6a. The linear regression derived from the MDR-EFR data is shown for both panels (black solid and dashed lines). The MDR-EFR relationship from the four WRF-Chem simulations is shown by the colored open circles, and the linear regression through these four markers is shown by the red dashed line. The slope, Pearson correlation coefficient and two-sided p value (for a hypothesis test whose null hypothesis is that the slope is zero) are reported for each regression line.

that the regional combustion efficiency that is detected with TROPOMI is generally consistent with the worldwide spatial distribution of EFs used by GFED4s (mostly based on Akagi et al., 2011). For the savanna fires we have consistently the highest estimates for MDR and EFR. The MDR and EFR for tropical deforestation fires are about half those of savanna fires. The peatland fires in turn have 3 times lower MDR and EFR. The lowest values in MDR and EFR (4 times lower than savanna fires), which suggest the least efficient type of biomass combustion, are shown for the North American and Siberian boreal regions. Note that the retrieved linear relationship in Fig. 7a between GFED4s EFR and TROPOMI MDR is similar to the linear relationship and slope found between EFR and MDR based on the four synthetic WRF-Chem simulations. Even with the aforementioned caveat that these simulations are simple in design, it does demonstrate quite convincingly that satellite and ground-based measurements of trace gas ratios are related to one another through a simple linear relationship.

The pattern of combustion signatures in MDR is somewhat different from EFR of GFAS (see Fig. 7b), which is mostly based on the older set of EFs from Andreae and Merlet (2001). The Pearson correlation coefficient between MDR and EFR is lower ($r = 0.49$) and the slope across the different fire regions is less steep. One reason is that the boreal fire characteristics in GFAS were lumped together with the temperate fires into a single category called extratropical fires, which reflects a much smaller smoldering combustion component and thus a higher EFR (see Table 1). As a consequence, Siberian boreal NO_x emissions are in GFAS ap-
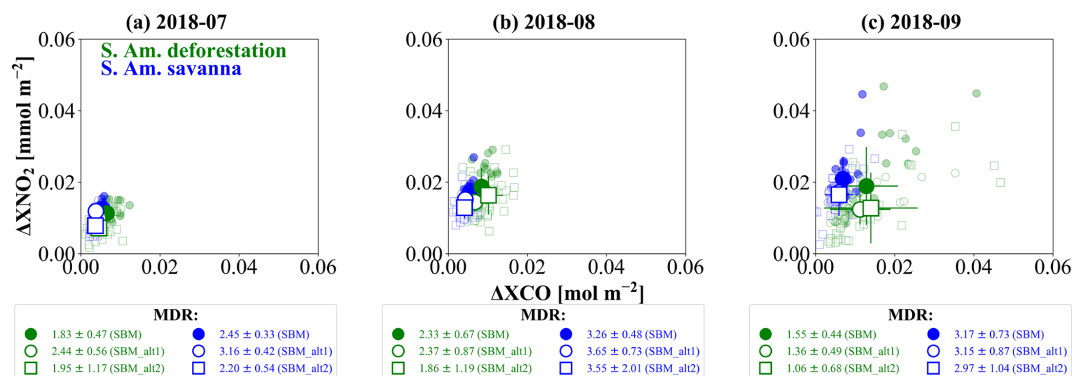
Figure 8. The relationship between daily ΔXCO (mol m^{-2}) and ΔXNO$_2$ (mmol m^{-2}) from TROPOMI for the South American deforestation (green) and savanna (blue) region for 3 consecutive months in 2018: July in panel **(a)**, August in panel **(b)** and September in panel **(c)**. For each month estimates are shown for three different sampling methods: SBM (solid circles), SBM_alt1 (open circles), and SBM_alt2 (open squares). In addition, the monthly average relationship between ΔXCO and ΔXNO$_2$ is depicted by the bigger markers together with error bars to indicate the 1σ day-to-day variability. The legend of each panel includes monthly average MDR and 1σ day-to-day variability estimates for each region and sampling method.

proximately 4 times larger than in GFED4s. This confirms the findings in the CAMS validation activity: comparisons with GOME-2 indicated largely overestimated boreal NO$_2$ concentrations in the CAMS forecasts driven by GFAS (Ramonet et al., 2019). Another reason for the mismatch is that the combustion efficiency of savanna fires in GFAS is on the same order of magnitude as the combustion efficiency in the boreal regions, which seems less realistic given the current body of EFs measurements from savanna ecosystems that claim the contrary. For peatland fires in Borneo, Indonesia, GFAS assumes a much larger fraction of smoldering combustion than GFED4s also. This large fraction of smoldering combustion would probably be more accurate during the drier years, e.g., during El Niño, than for the relatively wet year 2018.

3.2 South American deforestation and savanna fire characteristics

The joint analysis of ΔXCO and ΔXNO$_2$ column densities in Fig. 8a–c shows a clear distinction between the deforestation and savanna regions during the 3-month dry season. For the deforestation burning region we observe much larger increased levels of ΔXCO (up to 0.030 mol m^{-2}) relative to ΔXNO$_2$, mostly in September, indicating a substantial fraction of smoldering combustion later in the season. This is consistent with ground-based measurements of tropical forest fires that usually show a persistent smoldering phase that can continue for days, in particular when woody debris is ignited that is piled together (Carvalho et al., 2001; Morton et al., 2008). The day-to-day variability in ΔXCO is large but remains quite proportional to the variability in ΔXNO$_2$ in September, indicating that the relative amount of smoldering and flaming combustion remains relatively constant throughout the month. For the deforestation region ΔXCO

and ΔXNO$_2$ are correlated in September with Pearson correlation coefficients of $r = 0.82$, $r = 0.84$, and $r = 0.68$ for, respectively, the SBM, SBM_alt1 and SBM_alt2. The estimates of ΔXNO$_2$ are quite similar for the deforestation and the savanna region (between 0.005 and 0.05 mmol m^{-2}). However, lower ΔXCO values (up to 0.010 mol m^{-2}) point to a much cleaner combustion of savanna biomass, which is common for savanna fires, where the flaming phase typically dominates (Andreae and Merlet, 2001). In contrast to deforestation fires, ΔXCO and ΔXNO$_2$ for savanna fires are less correlated ($r < 0.66$); i.e., the trace gases do not change consistently on a day-to-day timescale.

In September, at the peak of the fire season, the monthly average MDR is significantly different for the two fire types, irrespective of the sampling method used (see Fig. 8c). The MDR estimates for deforestation fires range between 1.06 and 1.55, whereas the MDR estimates for savanna fires are higher, ranging between 2.97 and 3.17. The separation between deforestation and savanna fires remains also quite robust to the different bulk sampling methods used (SBM, SBM_alt1 or SBM_alt2). For each fire type, the monthly average ΔXCO and ΔXNO$_2$ estimates of the three sampling methods lay well within the 1σ uncertainty level of each method (the standard deviation of day-to-day variability in ΔXCO and ΔXNO$_2$). The differences in MDR between the SBM and SBM_alt1 are quite small in August and September (within 15 % for both fire types), indicating that the SBM is not so sensitive to a possibly non-Gaussian shape of the distribution. Much larger differences in MDR exist between the SBM and SBM_alt2 (up to 35 % for deforestation fires), with much larger day-to-day variability in MDR using SBM_alt2. It indicates the background estimates of XCO and XNO$_2$ in the adjacent regions are not necessarily consistent with the background densities derived with the Gaussian fit. These uncertainties can be attributed to the incorrect assump-
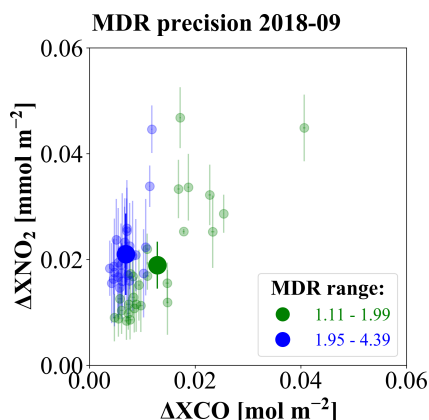
Figure 9. The relationship between daily $\Delta X\mathrm{CO}$ (mol m^{-2}) and $\Delta X\mathrm{NO}_2$ (mmol m^{-2}) from TROPOMI for the South American deforestation (green) and savanna (blue) region for September 2018 using the SBM. The error bars depict the range in $\Delta X\mathrm{CO}$ and $\Delta X\mathrm{NO}_2$ estimates induced by the instrument measurement precision. The range in $\Delta X\mathrm{NO}_2$ is larger than $\Delta X\mathrm{CO}$ because relatively, the $X\mathrm{NO}_2$ instrument precision is less accurate than $X\mathrm{CO}$. The legend reports the range of values in the monthly average MDR for both regions.

Figure 10. September 2018 daily estimates of $\Delta X\mathrm{CO}$ (mol m^{-2}) and $\Delta X\mathrm{NO}_2$ (mmol m^{-2}) from TROPOMI derived with the SBM, together with smoothed estimates of the MDR (colored dashed line), and smoothed CO emission estimates (GgCO region^{-1} d^{-1}) from GFED4s (black solid line) and GFAS (black dashed line). Panel **(a)** shows the results for the South American deforestation region and panel **(b)** for the South American savanna region.

tion that the sampled trace gases are Gaussian distributed or to the somewhat arbitrary choice of the background regions for SBM_alt2, which do not necessarily characterize the true background of each day in September. As discussed in Sect. 2.3.1, it is not our goal to determine the best possible background estimate, which is difficult for these kinds of regions that are continuously surrounded by fires. Instead, we opted for a mathematical method that is consistent in application for both trace gases and provides a reasonable proxy for regional fire-induced trace gas enhancements.

The influence of instrument precision on the $\Delta X\mathrm{CO}$, $\Delta X\mathrm{NO}_2$ and MDR estimates was also quantified. The instrument precision of $X\mathrm{CO}$ under relatively clear-sky conditions is primarily a function of surface albedo (Landgraf et al., 2016). The low albedo of the tropical deforestation region yields an average $X\mathrm{CO}$ precision of 0.0014 mol m^{-2}, which is 2 times larger than for the savanna region with an average $X\mathrm{CO}$ precision of 0.0007 mol m^{-2}. The precision of $X\mathrm{NO}_2$ is around 0.011 mmol m^{-2} for both regions and is dominated by air mass factor uncertainties under polluted conditions (Lorente et al., 2017). The contribution of instrument/retrieval precision to the uncertainty in $\Delta X\mathrm{CO}$, $\Delta X\mathrm{NO}_2$ and MDR was estimated using a synthetic distribution of daily measurements for both trace gases in September 2018. This was done as follows: assuming no systematic errors or biases, each single TROPOMI measurement was randomly perturbed by its precision value or decreased by its precision value or remained unchanged. Subsequently, the SBM was applied on this distribution, yielding an uncertainty range around $\Delta X\mathrm{CO}$, $\Delta X\mathrm{NO}_2$ and MDR values due to instrument or retrieval noise (see Fig. 9). While the $X\mathrm{NO}_2$

uncertainty is quite substantial in comparison to $X\mathrm{CO}$, their contribution to $\Delta X\mathrm{NO}_2$, and in the resulting MDR, it is actually quite small on a monthly timescale. There is barely any overlap in the range of monthly MDR estimates of the deforestation and savanna fires, which means that differences in combustion characteristics easily exceed the precision. Only for smaller $\Delta X\mathrm{CO}$ and $\Delta X\mathrm{NO}_2$ values will TROPOMI's precision become a more limiting factor in terms of signal-to-noise ratio and could explain the lower correlation between daily $\Delta X\mathrm{CO}$ and $\Delta X\mathrm{NO}_2$ noted before for savanna fires.

The September daily estimates of $\Delta X\mathrm{CO}$ and $\Delta X\mathrm{NO}_2$ are shown in Fig. 10a for the deforestation region along with the smoothed estimates of the MDR and the smoothed GFED4s and GFAS CO fire emissions. In September, when the enhancements of the two trace gases and the CO emissions are at their maximum, the MDR is also at its lowest level around 1.5, indicating persistent, less efficient combustion in the region (relatively less NO$_2$ and more CO release into the atmosphere). The same set of daily estimates are also shown for the savanna region in Fig. 10b. The peaks in $\Delta X\mathrm{CO}$ and $\Delta X\mathrm{NO}_2$ correspond to peaks in the GFAS CO emissions, and the MDR is quite constant between 3.0 and 3.5, i.e., about twice as high as the MDR for the deforestation region.

It is worthwhile noting that the GFAS and GFED4s emission products do not necessarily align well in Fig. 10a and b. As mentioned in Sect. 2.1, these two products use different methods and data products to derive fire emission estimates. The difference between GFAS and GFED4s reflects the uncertainty in the amount of CO emitted. This is apparent for
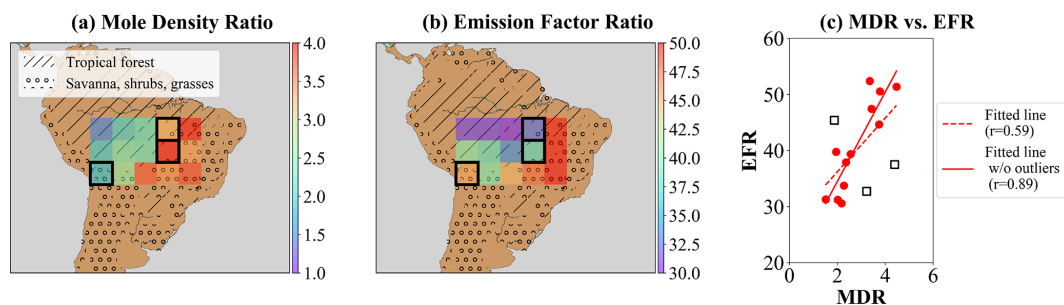
Figure 11. In panel **(a)** the spatial pattern of the September average MDR determined with TROPOMI for 15 $5° \times 5°$ regions using the SBM. In panel **(b)** for the same 15 regions the spatial pattern of the September average EFR determined from the ratio between NO_x and CO emissions from GFED4s. Panel **(c)** shows the relationship between the 15 MDR and EFR estimates, including the dashed linear regression line and the Pearson correlation coefficient. The three largest outliers are identified with a black square symbol and are highlighted by the black frames in panels **(a)** and **(b)**. The linear regression line without the outliers is shown by the solid line in panel **(c)**.

the savanna region, where the daily GFAS CO emissions are on average a factor of 4 larger than the GFED4s emissions. The 2018, GFED4s estimates are derived using active fire detections and their FRP and a simple relationship based on the climatological FRP and GFED4s ratio based on the 2003–2016 period for each $0.25° \times 0.25°$ grid cell. GFAS, on the other hand, used the FRP associated with those active fires and is tuned to match GFED3 emissions, not for each grid cell, but for each biome (Kaiser et al., 2012). In addition, the used EFs between the two products are different (see Table 1). For the large deforestation fires the estimates of CO emissions from GFAS and GFED4s are more similar, although the timing is somewhat different (see Fig. 10a).

We also demonstrate the detection of subcontinental-scale gradients in biomass burning efficiency from space. The September average MDR (derived with the standard SBM) is shown in Fig. 11a for 15 $5° \times 5°$ regions south of the Amazon River that cover the two main biomes: tropical rainforest (dominated by deforestation fires) and Cerrado savanna (dominated by savanna fires). For the same 15 regions we also derived the EFR from the monthly average GFED4s NO_x and CO fire emissions shown in Fig. 11b. These emissions are essentially based on the Akagi et al. (2011) EF database that is compiled from ground and airborne measurements. Although the relationship is not perfect, MDR responds fairly linearly to EFR ($r = 0.59$ shown in Fig. 11c). A very similar west–east relationship also exists between the 15 EFR estimates from GFAS and MDR ($r = 0.61$, not shown). However, GFAS EFR values are generally lower across the entire domain, which can be traced back to differences in EFs (see Table 1). In general, we see lower MDR and EFR values over the western part of the domain (where deforestation fires dominate) and higher MDR and EFR values over the eastern part of the domain (where savanna fires are more prevalent). The relationship becomes much more significant ($r = 0.89$) if three outliers are excluded from the analysis. One of these outliers represents a mountainous region in the southwestern corner of the domain, where fire activity was

much lower than elsewhere in the domain. The other two outliers represent regions that are located in between the tropical rainforest and the Cerrado savanna (highlighted in Fig. 11a and b). It is possible that the MDR and EFR do not align well at these locations because the biome-specific EFs are not representative of a more complex transition region. One would expect here more diversity in burning practices, vegetation types and climate conditions, resulting in a mixture of different burning characteristics that are not accounted for in the EF in either GFED4s or GFAS, which are based on coarser-resolution land cover data. Another factor that plays a role is atmospheric transport, as it affects the column mole densities that are measured downwind of the dominant fire type. The wind direction was predominantly from the east in September (see Fig. 4) and could as well carry the savanna-like combustion characteristics from the easternmost regions more towards the west (see Fig. 11a).

4 Discussion

In this paper, we demonstrated the capability of new high-quality XCO and XNO$_2$ column observations from the space-borne TROPOMI instrument to detect and quantify spatial variations in biomass combustion efficiency from a top-down perspective. The TROPOMI observations of XCO and XNO$_2$ (a good proxy for NO_x) and the MDR between the local enhancements of the two species have an important advantage over ground or airborne-based measurements due to the daily global spatial coverage, and as such are complementary to bottom-up derived EFR signatures.

We found distinct spatial patterns in MDR across different regions and continents which signify very different combustion efficiency characteristics. Irrespective of the utilized sampling method, these patterns in MDR compare well with EFR signatures around the world from existing fire emission datasets. In principle, these findings are not new but confirm from a remote sensing perspective the general spatial distribution of combustion efficiency of the current body of

EF measurements. Based on the TROPOMI measurements of just 1 year, we derived a first (but still preliminary) linear relationship between TROPOMI column observations of CO and NO$_2$ and EFs of CO and NO$_x$ near the fire source (see Fig. 7). This approach provides an additional anchor to help constrain combustion characteristics and can for instance be used to estimate and quantify the spatiotemporal variability of combustion efficiency around the world, even over regions where there is a deficiency of detailed information on fuel load, combustion practice and EFs.

The combustion in all savanna regions in South America, Africa and Australia was consistently cleaner and more efficient (i.e., highest MDR) than for all the other regions investigated. The MDR for Australia was determined by studying individual fire plumes with LSM and yielded the highest MDR estimate but also the largest day-to-day uncertainty. The other three savanna regions were determined with the SBM and yielded smaller MDR values but were still significantly larger than the MDRs derived for the other fire types. The LSM may be inclined to higher MDRs because ΔXNO$_2$ is derived from mole density measurements in close proximity to the actual fire sources where XNO$_2$ is at its highest level before any significant removal with OH occurs. On the other hand, the area sampled was very arid and mostly consisted of grasses. Therefore, smoldering combustion products like CO and CH$_4$ tend to be lower (Hurst et al., 1994). Our study also shows a relatively clean combustion process for the northern and southern African savanna fires, in agreement with the current EF datasets. In contrast to Zheng et al. (2018), we did not find evidence of a seasonal transition from flaming to smoldering combustion for the different African regions. They inverted multi-year XCO column measurements from the MOPITT instrument and found that GFED4s significantly underestimates the CO emissions by 12 % to 62 % later in the fire season. They partly attributed this outcome to the static EFs that are currently in use that omit seasonal variations in burning conditions. We therefore argue that the underestimation of GFED4s CO emissions is more likely the result of missing burned area detections in the late dry season.

In comparison to the savanna fires, lower MDR values were derived for the South American deforestation regions, indicating a larger contribution from smoldering combustion of organic soils and woody debris that is piled together at the surface. These spatial differences in combustion efficiency between deforestation and savanna fires agree with the study of Silva and Arellano (2017); however, a one-on-one comparison between the two studies is difficult. They derived estimates of MDR based on the ratio of ΔXCO/ΔXNO$_2$ (instead of ΔXNO$_2$ / ΔXCO), and they did their analysis for a different year, probably under somewhat different meteorological and chemistry regimes.

The least efficient type of combustion with the lowest MDR values was detected for the Indonesian peatland fires and boreal fires of North America and Siberia. In Indonesia, peatland fires are a recurring seasonal phenomenon that generates severe atmospheric pollution and impacts public health (Marlier et al., 2013). In many lowland regions, forest clearing occurs along with drainage of peat-swamp forest, exposing peat to fire. During the dry season, the boreal forest fires consume large amounts of above- and especially below-ground biomass, including the burning of organic soils, peat, and woody debris (Ottmar and Sandberg, 2003; French et al., 2004). Typically, such ecosystems burn by residual smoldering combustion which can continue long after the initial flaming phase of the fires (Akagi et al., 2011).

The difference in MDRs between the North American and Siberian boreal fires in Fig. 6a suggests different fire dynamics between the two boreal regions. These differences do not appear in the EFR estimates of GFAS and GFED4s because the EF datasets lack spatial and temporal variability for each fire type. The lower average MDR value for Siberia indicates generally more smoldering combustion (less NO$_x$, more CO) than the combustion in North America. This result supports independently the findings of Wooster and Zhang (2004) and Rogers et al. (2015), who found compelling evidence of smaller fire intensity and burn severity in the Siberian boreal forests across multiple satellite datasets (but not TROPOMI) and forest inventories. Rogers et al. (2015) related the differences in fire dynamics between these two regions to their dominant tree species. Pine trees in Eurasia have evolved to resist and suppress crown fires. Therefore, the fires in these areas are usually reported as surface fires, which burn mostly in the smoldering phase. The trees in the northern parts of North America have evolved to spread and be consumed by more intense crown fires, killing most trees. Yet we remain cautious to fully attribute the detected differences between the North American and Siberian MDR to the burning characteristics of specific tree species until we have analyzed multiple years of TROPOMI data. The uncertainties in MDR for 2018 (based on day-to-day variability) are still quite substantial for the boreal regions, as is shown in Fig. 6a.

Our estimates of MDR across the world compared most favorably with the spatial distribution of biomass burning efficiency prescribed in GFED4s, where the proxy of efficiency is carried through the EFs of CO and NO$_x$. The remotely sensed measurements confirm the addition of a dedicated boreal forest fire type as a key improvement that was implemented in the more recent Akagi et al. (2011) EF database (used by GFED4s). It underlines the need for EFs that reflect a large component of smoldering combustion of organic soils and boreal peat in this part of the world (Yokelson et al., 1997; Bertschi et al., 2003). This was specifically done in the Akagi et al. (2011) EF dataset, where they applied an equal weighting scheme for the boreal region airborne measurements (which have a bias towards flaming fires) and ground-based measurements (which have a bias towards smoldering fires). Our MDR estimate for the two Indonesian peatland regions is lower than MDR for deforestation fires but higher than the MDR for boreal fires. Therefore, it is likely

that it represents a combination of peat soil combustion (usually consumed almost entirely by smoldering) and overstory combustion of tropical forests, grasslands, and agriculture (usually consumed by flaming and smoldering). This relative pattern is in agreement with a more mixed combustion efficiency prescribed in GFED4s for Indonesia (for both Borneo and Sumatra). The Borneo fires in GFAS exhibited a much larger smoldering component, which may be more common during El Niño years when fires spread out of control, consuming a significant portion of the underlying peat soils. However, 2018 was not an El Niño year, and evidence of excessive smoldering combustion was not found in the TROPOMI data (see Fig. 6a). In fact, the TROPOMI data suggest more complete combustion efficiency in Borneo than in Sumatra (1.43 vs. 0.94 MDR).

The day-to-day variations in MDR (shown in Fig. 6a) point to a considerable amount of uncertainty. An important source of this uncertainty is first of all the SBM sampling method. Estimates of ΔXCO and ΔXNO$_2$ can deviate substantially on a daily basis depending on how much the sampled data are skewed to either side of the scale, away from a perfect Gaussian normal distribution. It was demonstrated for South American fires (see Fig. 8) that the SBM and the two alternative sampling methods can produce quite a range in MDR. Similarly, the instrument/retrieval precision of TROPOMI's XNO$_2$ was also a small source of uncertainty in MDR (see Fig. 9). However, regardless of the sampling method or precision, we were still able to distinguish clearly the deforestation fires from savanna fires using the monthly aggregated ΔXCO and ΔXNO$_2$ data. The alternative sampling methods were also used to derive MDR from the synthetic WRF-Chem simulations, and similarly, it did not deteriorate our ability to distinguish the four different fire types (not shown in the paper).

Another source of uncertainty in MDR is the difference in surface sensitivity of TROPOMI's XCO and XNO$_2$ measurements. A comparison of the column AK of both species shows that tropospheric XNO$_2$ measurements are generally less sensitive to sources in the planetary boundary layer than XCO measurements. From the surface to approximately 800 hPa the sensitivity of XNO$_2$ is smaller than for XCO but increases from the mid-troposphere to tropopause (800–200 hPa). This is one of the reasons why our daily estimates of ΔXNO$_2$ are biased low. Potentially, it has an effect on most of our MDR estimates because it has been demonstrated, using stereo-height measurements of smoke plumes, that most fires are typically emitted inside the planetary boundary layer (Martin et al., 2018). The estimates of ΔXCO, ΔXNO$_2$ and MDR derived from the simulated XCO and XNO$_2$ column data (WRF-Chem experiments in Figs. 6b and 7) were calculated with a daily region-average AK for September 2018. This provided more realistic column estimates for both species (and thus a more realistic MDR estimate) that allowed a better one-to-one comparison with TROPOMI MDR estimates, even under cloudy conditions (Borsdorff et al. 2018b). Not using the AKs to derive MDR with WRF-Chem, and instead simply using the simulated total XCO and the tropospheric XNO$_2$ column densities, would yield a higher MDR estimate. This is because simulated XNO$_2$ enhancements from surface fire sources are, in comparison to TROPOMI's limited measurement sensitivity in the PBL, unrealistically overrepresented in WRF-Chem.

In general, a large part of the biases in ΔXNO$_2$ (and thus in MDR), either caused by the sampling techniques or the precision and sensitivity, were in all likelihood somewhat similar in magnitude in the regions we studied. Hence, we believe it did not impair the detection of differences in fire characteristics. The uncertainty related to chemistry and transport may have played a larger role region to region as it affected tropospheric NO$_2$ more differently than CO and thus our ability to derive a robust MDR. In particular, on shorter day-to-day timescales the MDR estimates can vary greatly. The amount of OH radicals in the atmosphere acts as the primary daytime sink of NO$_2$ and can vary substantially depending on the amount of tropospheric O$_3$, water vapor and incoming sunlight (source of OH), and the presence of other chemical species such as volatile organic compounds (sink of OH). Overall, it reduces the lifetime of NO$_2$ to several hours, much shorter than the lifetime of CO. As a consequence, daily estimates of ΔXNO$_2$ will always be biased low. In addition, daily variations in ΔXNO$_2$ that are driven by transport and chemistry are naturally exacerbated in ΔXNO$_2/\Delta X$CO ratio space. Therefore, to interpret MDR, it is currently necessary to collect multiple days of data (e.g., for an entire month) to retrieve a more robust combustion efficiency signature that cancels out some of the day-to-day variations in transport and chemistry. Potentially we could minimize these variations retroactively by inverting the measured MDR back to a daily EFR estimate, where we take the removal of NO$_2$ into account. This could provide a more direct top-down estimate of EFR and could improve the detection of seasonal (and maybe even daily) changes in fire characteristics. For instance, the transition from flaming to more smoldering fires, as suggested to occur in the African savanna (Zheng et al., 2018), or the supposed differences between North American and Siberian boreal fires (Rogers et al., 2015) might be detected more easily that way. Future research could explore this but requires a more elaborate analysis for each region separately, with emphasis on acquiring a better understanding of the daily variations of regional OH content, wind speed and direction, and the chemical rate constant of NO$_2$ removal.

5 Conclusion

We have investigated regional biomass burning characteristics and efficiency using the new space-based TROPOMI measurements of XCO and XNO$_2$. The mole density ratios

(MDRs) between regional enhancements of $X\mathrm{NO}_2$ and $X\mathrm{CO}$ have been quantified using different sampling techniques, which have been tested using WRF-Chem simulations accounting for realistic atmospheric transport, chemistry and the limited instrument sensitivity to the lower atmosphere. TROPOMI provides independent support for the more recent Akagi et al. (2011) set of EFs used in fire emission products like GFED4s. We have found spatial variations in combustion efficiency that match the ground and airborne measurements of EFs quite accurately. Generally, boreal fires show a much larger fraction of smoldering combustion than savanna grassland and tropical deforestation fires (boreal ecosystems cause a 3 to 6 times larger increase in $\Delta X\mathrm{CO}$ than $\Delta X\mathrm{NO}_2$). On smaller spatial scales of a thousand kilometers, we also found gradients in combustion characteristics from west to east over Brazil. In the state of Amazonas, the practice of tropical deforestation, where woody debris after initial clearing is ignited during the dry season, is clearly distinguishable from fires in the savanna-like ecosystem in central Brazil, where fires mostly consume the grass layer by flaming combustion. We have found deforestation fires to cause a 1.5 to 2 times larger increase in $\Delta X\mathrm{CO}$ relative to $\Delta X\mathrm{NO}_2$ than the savanna fires, mainly because these fires reflect a larger fraction of surface smoldering combustion. The detected differences, interregional (e.g., boreal vs. savanna) and intraregional (e.g., North American vs. Eurasian boreal region), underline that TROPOMI can provide new top-down constraints on biomass burning characteristics and EFs.

Code and data availability. WRF-Chem atmospheric transport model version 4.0 can be downloaded from https://www2.mmm.ucar.edu/wrf/users/downloads.html (last access: 18 December 2020) (WRF, 2020).

TROPOMI measurements of NO$_2$ and CO can be downloaded from https://s5phub.copernicus.eu (last access: 18 December 2020) (ESA, 2020); GFED4s fire emissions can be downloaded from https://www.geo.vu.nl/~gwerf/GFED/GFED4/ (last access: 18 December 2020) (van der Werf, 2020); GFAS fire emissions can be downloaded from https://apps.ecmwf.int/datasets/data/cams-gfas/ (last access: 18 December 2020) (ECMWF, 2020).

Author contributions. IvdV did the data analysis, designed and ran the model simulations and wrote the paper. GvdW, SH, and IA provided science advice and detailed comments on the manuscript. HE, JPV, and TB provided additional comments on the manuscript and TROPOMI retrieval products.

Competing interests. The authors declare that they have no conflict of interest.

Special issue statement. This article is part of the special issue "TROPOMI on Sentinel-5 Precursor: first year in operation (AMT/ACP inter-journal SI)". It is not associated with a conference.

Review statement. This paper was edited by Jhoon Kim and reviewed by two anonymous referees.

References

Akagi, S. K., Yokelson, R. J., Wiedinmyer, C., Alvarado, M. J., Reid, J. S., Karl, T., Crounse, J. D., and Wennberg, P. O.: Emission factors for open and domestic biomass burning for use in atmospheric models, Atmos. Chem. Phys., 11, 4039–4072, https://doi.org/10.5194/acp-11-4039-2011, 2011.

Andreae, M. O., Browell, E. V., Garstang, M., Gregory, G. L., Harriss, R. C., Hill, G. F., Jacob, D. J., Pereira, M. C., Sachse, G. W., Setzer, A. W., Silvadias, P. L., Talbot, R. W., Torres, A. L., and Wofsy, S. C.: Biomass-burning emissions and associated haze layers over Amazonia, J. Geophys. Res., 93, 1509–1527, 1988.

Andreae, M. O. and Merlet, P.: Emission of trace gases and aerosols from biomass burning, Global Biogeochem. Cy., 15, 955–966, https://doi.org/10.1029/2000GB001382, 2001.

Andreae, M. O.: Emission of trace gases and aerosols from biomass burning – an updated assessment, Atmos. Chem. Phys., 19, 8523–8546, https://doi.org/10.5194/acp-19-8523-2019, 2019.

Bertschi, I. T., Yokelson, R. J., Ward, D. E., Babbitt, R. E., Susott, R. A., Goode, J. G., and Hao, W. M.: Trace gas and particle emissions from fires in large diameter and belowground biomass fuels, J. Geophys. Res., 108, 8472, https://doi.org/10.1029/2002JD002100, 2003.

Boersma, K. F., Eskes, H. J., Dirksen, R. J., van der A, R. J., Veefkind, J. P., Stammes, P., Huijnen, V., Kleipool, Q. L., Sneep, M., Claas, J., Leitão, J., Richter, A., Zhou, Y., and Brunner, D.: An improved tropospheric NO2 column retrieval algorithm for the Ozone Monitoring Instrument, Atmos. Meas. Tech., 4, 1905-1928, https://doi.org/10.5194/amt-4-1905-2011, 2011.

Boersma, K. F., Eskes, H. J., Richter, A., De Smedt, I., Lorente, A., Beirle, S., van Geffen, J. H. G. M., Zara, M., Peters, E.,

Van Roozendael, M., Wagner, T., Maasakkers, J. D., van der A, R. J., Nightingale, J., De Rudder, A., Irie, H., Pinardi, G., Lambert, J.-C., and Compernolle, S. C.: Improving algorithms and uncertainty estimates for satellite NO2 retrievals: results from the quality assurance for the essential climate variables (QA4ECV) project, Atmos. Meas. Tech., 11, 6651–6678, https://doi.org/10.5194/amt-11-6651-2018, 2018.

Borsdorff, T., aan de Brugh, J., Hu, H., Hasekamp, O., Sussmann, R., Rettinger, M., Hase, F., Gross, J., Schneider, M., Garcia, O., Stremme, W., Grutter, M., Feist, D. G., Arnold, S. G., De Mazière, M., Kumar Sha, M., Pollard, D. F., Kiel, M., Roehl, C., Wennberg, P. O., Toon, G. C., and Landgraf, J.: Mapping carbon monoxide pollution from space down to city scales with daily global coverage, Atmos. Meas. Tech., 11, 5507–5518, https://doi.org/10.5194/amt-11-5507-2018, 2018a.

Borsdorff, T., aan de Brugh, J., Hu, H., Aben, I., Hasekamp, O., and Landgraf, J.: Measuring Carbon Monoxide With TROPOMI: First Results and a Comparison With ECMWF-IFS Analysis Data, Geophys. Res. Lett., 10, 1769–1767, 2018b.

Carvalho Jr., J. A., Costa, F. S., Veras, C. A. G., Sandberg, D. V., Alvarado, E. C., Gielow, R., Serra Jr., A. M., and Santos, J. C.: Biomass fire consumption and carbon release rates of rainforest-clearing experiments conducted in northern Mato Grosso, Brazil, J. Geophys. Res., 106, 17877–17887, 2001.

Christian, T. J., Kleiss, B., Yokelson, R. J., Holzinger, R., Crutzen, P. J., Hao, W. M., Saharjo, B. H., and Ward, D. E.: Comprehensive laboratory measurements of biomass-burning emissions: 1. Emissions from Indonesian, African, and other fuels, J. Geophys. Res, 108, 4719, https://doi.org/10.1029/2003JD003704, 2003.

ECMWF: CAMS Global Fire Assimilation System dataserver, available at: https://apps.ecmwf.int/datasets/data/cams-gfas/, last access: 18 December 2020.

ESA: Sentinal-5p Pre-Operational Data Hub, available at: https://s5phub.copernicus.eu, last access: 18 December 2020.

Eskes, H. J. and Eichmann, K. U.: S5P Mission Performance Centre Nitrogen Dioxide [L2 __ NO2_ __] Readme document, S5P-MPC-KNMI-PRF-NO2, KNMI, available at: https://sentinel.esa.int/documents/247904/3541451/Sentinel-5P-Nitrogen-Dioxide-Level-2-Product-Readme-File (last access: 18 December 2020), 2018.

French, N. H. F., Goovaerts, P., and Kasischke, E. S.: Uncertainty in estimating carbon emissions from boreal forest fires, J. Geophys. Res., 109, D14S08, https://doi.org/10.1029/2003JD003635, 2004.

Giglio, L., Randerson, J. T., and van der Werf, G. R.: Analysis of daily, monthly, and annual burned area using the fourth-generation global fire emissions database (GFED4), J. Geophys. Res.-Biogeo., 118, 317–328, https://doi.org/10.1002/jgrg.20042, 2013.

Hassler, B., McDonald, B. C., Frost, G.J., Borbon, A., Carslaw, D. C., Civerolo, K., and Pollack, I. B.: Analysis of long-term observations of NO$_x$ and CO in megacities and application to constraining emissions inventories, Geophys. Res. Lett, 43, 9920–9930, 2016.

Hoelzemann, J. J., Schultz, M. G., and Brasseur, G. P.: Global Wildland Fire Emission Model (GWEM): Evaluating the use of global area burnt satellite data, J. Geophys. Res., 109, D14S04, https://doi.org/10.1029/2003JD003666, 2004.

Hong, S. and Lim, J.: The WRF Single-Moment 6-Class Microphysics Scheme (WSM6), J. Korean Meteor.l Soc., 42, 129–151, 2006.

Hu, X.-M., Klein, P. M., and Xue, M.: Evaluation of the updated YSU planetary boundary layer scheme within WRF for wind resource and air quality assessments, J. Geophys. Res.-Atmos., 118, 10490–10505, 2013.

Hurst, D. F., Griffith, D. W. T., and Cook, G. D.: Trace gas emissions from biomass burning in tropical Australian savannas, J. Geophys. Res., 99, 16441–16456, 1994.

Ito, A. and Penner, J. E.: Global estimates of biomass burning emissions based on satellite imagery for the year 2000, J. Geophys. Res., 109, D14S05, https://doi.org/10.1029/2003JD004423, 2004.

Kaiser, J. W., Heil, A., Andreae, M. O., Benedetti, A., Chubarova, N., Jones, L., Morcrette, J.-J., Razinger, M., Schultz, M. G., Suttie, M., and van der Werf, G. R.: Biomass burning emissions estimated with a global fire assimilation system based on observed fire radiative power, Biogeosciences, 9, 527–554, https://doi.org/10.5194/bg-9-527-2012, 2012.

Konovalov, I. B., Berezin, E. V., Ciais, P., Broquet, G., Zhuravlev, R. V., and Janssens-Maenhout, G.: Estimation of fossil-fuel CO$_2$ emissions using satellite measurements of "proxy" species, Atmos. Chem. Phys., 16, 13509–13540, https://doi.org/10.5194/acp-16-13509-2016, 2016.

Lacaux, J. P., Delmas, R., Jambert, C., and Kuhlbusch, T. A. J.: NO$_x$ emissions from African savanna fires, J. Geophys. Res., 101, 23585–23595, 1996.

Landgraf, J., aan de Brugh, J., Scheepmaker, R., Borsdorff, T., Hu, H., Houweling, S., Butz, A., Aben, I., and Hasekamp, O.: Carbon monoxide total column retrievals from TROPOMI shortwave infrared measurements, Atmos. Meas. Tech., 9, 4955–4975, https://doi.org/10.5194/amt-9-4955-2016, 2016.

Landgraf, J., Borsdorff, T., Langerock, B., and Keppens, A.: S5P Mission Performance Centre Carbon Monoxide [L2__CO_ _ __] Readme document, S5P-MPC-SRON-PRF-CO, SRON, available at: https://sentinel.esa.int/documents/247904/3541451/Sentinel-5P-Carbon-Monoxide-Level-2-Product-Readme-File (last access: 18 December 2020), 2018.

Lopez, M., Schmidt, M., Delmotte, M., Colomb, A., Gros, V., Janssen, C., Lehman, S. J., Mondelain, D., Perrussel, O., Ramonet, M., Xueref-Remy, I., and Bousquet, P.: CO, NO$_x$ and ^{13}CO$_2$ as tracers for fossil fuel CO$_2$: results from a pilot study in Paris during winter 2010, Atmos. Chem. Phys., 13, 7343–7358, https://doi.org/10.5194/acp-13-7343-2013, 2013.

Lorente, A., Folkert Boersma, K., Yu, H., Dörner, S., Hilboll, A., Richter, A., Liu, M., Lamsal, L. N., Barkley, M., De Smedt, I., Van Roozendael, M., Wang, Y., Wagner, T., Beirle, S., Lin, J.-T., Krotkov, N., Stammes, P., Wang, P., Eskes, H. J., and Krol, M.: Structural uncertainty in air mass factor calculation for NO$_2$ and HCHO satellite retrievals, Atmos. Meas. Tech., 10, 759–782, https://doi.org/10.5194/amt-10-759-2017, 2017.

Marlier, M. E., DeFries, R. S., Voulgarakis, A., Kinney, P. L., Randerson, J. T., Shindell, D. T., Chen, Y., and Faluvegi, G.: El Niño and health risks from landscape fire emissions in southeast Asia, Nat. Clim. Chang. 3, 131–136, 2013.

Martin, M. V., Kahn, R. A., and Tosca, M. G.: A global analysis of wildfire smoke injection heights derived from

space-based multi-angle imaging, Remote Sens., 10, 1609, https://doi.org/10.3390/rs10101609, 2018.

Mebust, A. K. and Cohen, R. C.: Observations of a seasonal cycle in NO_x emissions from fires in African woody savannas, Geophys. Res. Lett., 40, 1451–1455, https://doi.org/10.1002/grl.50343, 2013.

Mlawer, E. J., Taubman, S. J., Brown, P. D., Iacono, M. J., and Clough, S. A.: Radiative transfer for inhomogeneous atmospheres: RRTM, a validated correlated-k model for the longwave, J. Geophys. Res.-Atmos., 102, 16663–16682, 1997.

Morton, D. C. Defries, R. S., Randerson, J. T., Giglio L., Schroeder, W., and van der Werf, G. R.: Agricultural intensification increases deforestation fire activity in Amazonia, Glob. Change Biol., 14, 2262–2275, https://doi.org/10.1111/j.1365-2486.2008.01652.x, 2008.

Ottmar, R. D. and Sandberg, D. V.: Predicting forest floor consumption from wildland fire in boreal forests of Alaska – preliminary results, Proceedings of Fire Conference 2000: The first national congress on fire ecology, prevention, and management, edited by: Galley, K. E. M., Klinger, R. C., and Sugihara, N. G., Miscellaneous Publication No. 13, Tall Timbers Research Station, Tallahassee, FL, 218–224, 2003.

Peters, W., Jacobson, A. R., Sweeney, C., Andrews, A. E., Conway, T. J., Masarie, K., Miller, J. B., Bruhwiler, L. M. P., Petron, G., Hirsch, A. I., Worthy, D. E. J., van der Werf, G. R., Randerson, J. T., Wennberg, P. O., Krol, M. C., and Tans, P. P.: An atmospheric perspective on North American carbon dioxide exchange: CarbonTracker, P. Natl. Acad. Sci., 104, 18925–18930, https://doi.org/10.1073/pnas.0708986104, 2007.

Potter, C. S., Randerson, J. T., Field, C. B., Matson, P. A., Vitousek, P. M., Mooney, H. A., and Klooster, S. A.: Terrestrial Ecosystem Production – a Process Model-Based on Global Satellite and Surface Data, Global Biogeochem. Cy., 7, 811–841, https://doi.org/10.1029/93GB02725, 1993.

Ramonet, M., Wagner, A., Schulz, M., Christophe, Y., Eskes, H. J., Basart, S., Benedictow, A., Bennouna, Y., Blechschmidt, A.-M., Chabrillat, S., Cuevas, E., El-Yazidi, A., Flentje, H., Hansen, K. M., Im, U., Kapsomenakis, J., Langerock, B., Richter, A., Sudarchikova, N., Thouret, V., Warneke, T., and Zerefos, C.: Validation report of the CAMS near-real-time global atmospheric composition service: Period June–August 2019, Copernicus Atmosphere Monitoring Service (CAMS) report, https://doi.org/10.24380/def9-na43, 2019.

Randerson, J. T., Chen, Y., van der Werf, G. R., Rogers, B. M., and Morton, D. C.: Global burned area and biomass burning emissions from small fires, J. Geophys. Res.-Biogeo., 117, G04012, https://doi.org/10.1029/2012JG002128, 2012.

Reuter, M., Ryerson, T. B., Trainer, M., Neuman, J. A., Roberts, J. M., and Parrish, D. D.: Decreasing emissions of NO_x relative to CO_2 in East Asia inferred from satellite observations, Nat. Geosci., 7, 792–795, 2014.

Rogers, B. M., Soja, A. J., Goulden, M. L., and Randerson, J. T.: Influence of tree species on continental differences in boreal fires and climate feedbacks, Nat. Geosci., 8, 228–234, https://doi.org/10.1038/NGEO2352, 2015.

Silva, S. J., Arellano, A. F., and Worden, H.: Toward anthropogenic combustion emission constraints from space-based analysis of urban CO_2/CO sensitivity, Geophys. Res. Lett., 40, 4971–4976, 2013.

Silva, S. J. and Arellano, A. F.: Characterizing regional-scale combustion using satellite retrievals of CO, NO_2 and CO_2, Remote Sens., 9, 744, 2017.

Stockwell, W. R., Middleton, P., and Chang, J. S.: The second generation regional acid deposition model chemical mechanism for regional air quality modeling, J. Geophys. Res., 95, 16343–16367, 1990.

Tiedtke, M.: A comprehensive mass flux scheme for cumulus parameterization in large–scale models, Mon. Weather Rev., 117, 1779–1800, 1989.

van Geffen, J. H. G. M., Boersma, K. F., Van Roozendael, M., Hendrick, F., Mahieu, E., De Smedt, I., Sneep, M., and Veefkind, J. P.: Improved spectral fitting of nitrogen dioxide from OMI in the 405–465 nm window, Atmos. Meas. Tech., 8, 1685–1699, https://doi.org/10.5194/amt-8-1685-2015, 2015.

van Leeuwen, T. T., Peters, W., Krol, M. C., and van der Werf, G. R.: Dynamic biomass burning emission factors and their impact on atmospheric CO mixing ratios, J. Geophys. Res.-Atmos., 118, 6797–6815, https://doi.org/10.1002/jgrd.50478, 2013.

van der Werf, G. R., Randerson, J. T., Collatz, G. J., and Giglio, L.: Carbon emissions from fires in tropical and subtropical ecosystems, Glob. Change Biol., 9, 547–562, 2003.

van der Werf, G. R., Randerson, J. T., Giglio, L., Collatz, G. J., Mu, M., Kasibhatla, P. S., Morton, D. C., DeFries, R. S., Jin, Y., and van Leeuwen, T. T.: Global fire emissions and the contribution of deforestation, savanna, forest, agricultural, and peat fires (1997–2009), Atmos. Chem. Phys., 10, 11707–11735, https://doi.org/10.5194/acp-10-11707-2010, 2010.

van der Werf, G.: GFED4 download page, available at: https://www.geo.vu.nl/~gwerf/GFED/GFED4/, last access: 18 December 2020.

van der Werf, G. R., Randerson, J. T., Giglio, L., van Leeuwen, T. T., Chen, Y., Rogers, B. M., Mu, M., van Marle, M. J. E., Morton, D. C., Collatz, G. J., Yokelson, R. J., and Kasibhatla, P. S.: Global fire emissions estimates during 1997–2016, Earth Syst. Sci. Data, 9, 697–720, https://doi.org/10.5194/essd-9-697-2017, 2017.

Veefkind, J. P., Aben, I., McMullan, K., Förster, H., de Vries, J., Otter, G., Claas, J., Eskes, H. J., de Haan, J. F., Kleipool, Q., van Weele, M., Hasekamp, O., Hoogeveen, R., Landgraf, J., Snel, R., Tol, P., Ingmann, P., Voors, R., Kruizinga, B., Vink, R., Visser, H., and Levelt, P. F.: TROPOMI on the ESA Sentinel-5 Precursor: A GMES mission for global observations of the atmospheric composition for climate, air quality and ozone layer applications, Remote Sens. Environ., 120, 70–83, https://doi.org/10.1016/j.rse.2011.09.027, 2012.

Wooster, M. J. and Zhang, Y. H.: Boreal forest fires burn less intensely in Russia than in North America. Geophys. Res. Lett., 31, L20505, https://doi.org/10.1029/2004GL020805O, 2004.

WRF: WRF model version 4, available at: https://www2.mmm.ucar.edu/wrf/users/downloads.html, last access: 18 December 2020.

Yokelson, R. J., Susott, R., Ward, D. E., Reardon, J., and Griffith, D. W. T.: Emissions from smoldering combustion of biomass measured by open-path Fourier transform infrared spectroscopy, J. Geophys. Res., 102, 18865–18877, https://doi.org/10.1029/97JD00852, 1997.

Yokelson, R. J., Susott, R., Ward, D. E., Reardon, J., and Griffith, D. W. T.: Emissions of formaldehyde, acetic acid, methanol, and other trace gases from biomass fires in North Carolina measured by airborne Fourier transform infrared spectroscopy, J. Geophys. Res., 104, 30109–30125, 1999.

Zheng, B., Chevallier, F., Ciais, P., Yin, Y., and Wang, Y.: On the role of the flaming to smoldering transition in the seasonal cycle of African fire emissions, Geophys. Res. Lett., 45, 11998–12007, https://doi.org/10.1029/2018GL079092, 2018.